LDA EXPERIMENTS ON A MIXING LAYER

H.W. van den Brink

Delft University of Technology
Department of Applied Physics

Delft, March 1998

Kramers Laboratorium voor
Fysische Technologie
Prins Bernhardlaan 6
2628 BW Delft

Professor: Prof. dr. ir. H.E.A. van den Akker
Supervisors: Dr. R.F. Mudde
Ir. D. Lathouwers

Summary

Investigation on plane turbulent two phase mixing layers serves to get insight in the mutual interaction between the behaviour of the injected gas bubbles and the turbulence of the liquid phase.

An experimental setup for investigations on such a mixing layer has been built. The measuring section is 20 cm in depth, 40 cm in width, and 150 cm in height. Measurements have been done on the liquid phase (water) with use of Laser Doppler Anemometry. These measurements mainly serve to determine the quality of the setup.
The LDA measurements relate, first, to averaged velocities and their profiles, and second, to turbulent quantities, viz. rms values and uv-stresses.
From the turbulent quantities, 1D-spectra and autocorrelation functions have been determined.
As a direct result of the measurements, the air distribution was improved.

The experimental results indicate that a leakage between the two sections exists. This should be repaired, along with the obliquity of the splitter plate.
To get more reliable spectra, the data rate of the LDA measurements has to be increased.
Another requirement for future measurements is the use of an accurate and more stable traverse system for the LDA probe.

Samenvatting

Onderzoek aan vlakke turbulente tweefasen menglagen dient om inzicht te verkrijgen in de onderlinge interactie tussen het gedrag van de geïnjecteerde gasbellen en de turbulentie van de vloeistoffase.

Een experimentele opstelling voor onderzoek aan zo'n menglaag is gebouwd. De meetsectie is 20 cm diep, 40 cm breed en 150 cm hoog. Metingen zijn verricht aan de vloeistoffase (water) met behulp van Laser Doppler Anemometrie. De gedane metingen dienen voornamelijk om de kwaliteit van de opstelling te bepalen.
De LDA metingen hebben ten eerste betrekking op de gemiddelde snelheden en hun profielen, en ten tweede, op turbulente grootheded, zoals rms waarden en uv-stressen.
Van de turbulente grootheden zijn 1D-spectra en autocorrelatie functies bepaald.
De gas distributie is verbeterd naar aanleiding van metingen.

De gevonden experimentele uitkomsten geven aan dat er een lek is tussen beide compartimenten. Dit dient verholpen te worden, evenals de scheve stand van de splitplaat.
Om meer betrouwbare spectra te verkrijgen, dient de data rate van de LDA metingen verhoogd te worden.
Een andere vereiste voor toekomstige metingen is het gebruiken van een nauwkeurige en meer stabiele traverseerinrichting voor de LDA probe.

List of Symbols

Roman symbols

Symbol	Description	Unity
A	Surface of intersection	m^2
B	Width of the mixing zone	m
c	Velocity of light in vacuum	m/s
c_k	Fourier coefficients	m/s
C_D	Drag coefficient	-
d_f	Fringe spacing	m
d_0	Diameter of the laser beams at intersection point	m
d_m	Length of short axis of measuring volume	m
D_0	1) Equivalent diameter	m
	2) Diameter of the laser beam	m
D_1	Diameter of wire	m
D_2	Diameter of tube	m
D_h	Hydraulic diameter	m
D_{mean}	Mean diameter of bubbles	m
f	1) Friction factor	-
	2) Frequency	Hz
f_D	Beat frequency	Hz
f_K	Kolmogorov frequency	Hz
f_{Nyq}	Nyquist frequency	Hz
f_s	Frequency of scattered light detected by the observer	Hz
f_{shift}	Preshift frequency	Hz
f_0	Frequency of the light emitted by the source	Hz
Δf	Sample frequency step	Hz
F	Focal distance of probe lens	m
$\mathcal{F}(x)$	Fourier transform of x	-
$\mathcal{F}^*(x)$	Complex conjugate of the Fourier transform of x	-
$h(\omega)$	Normalised power spectral density function	s
$H(k)$	Hanning filter	-
$H(\tau_k)$	Number of cross products within k^{th} slot	-
I	Turbulence intensity	%
I_x	Component of turbulence intensity in x-direction	%

j	Imaginary number	-
k	Counter	-
l_m	Length of long axis of measuring volume	m
l_w	Length scale associated with the dissipation of the fluctuations in the wake of a bubble	m
L	1) Characteristic length scale	m
	2) Length of tube	m
L_{mean}	Mean intersection length of bubbles	m
L_{ref}	Reference length of probe tip	m
m	1) Counter	-
	2) Number of blocks	-
M	Number of slots	-
N	Number of samples	-
p	Pressure	N/m^2
Δp	Pressure drop	N/m^2
$R(\tau)$	Autocovariance function	m^2/s^2
$R_{1,2}$	Radii of curvatures	m
$S(\omega)$	Power spectral density function	m^2/s
T_{gas}	Time that fibre probe is surrounded by gas	s
T_{total}	Total gas fraction measurement time	s
Δt	slot width	s
T	Total measuring time	s
$\mathcal{T}$	Integral time scale	s
u_*	friction velocity	m/s
u_m	Vertical component of nth measurement	m/s
$u_{m,n}$	nth measurement of velocity in vertical probe direction	m/s
u'_w	Fluctuating velocity in the wake of a bubble	m/s
U_1	Mean velocity at the right section	m/s
U_2	Mean velocity at the left section	m/s
U_m	Mean velocity of U_1 and U_2	m/s
U_R	Rise velocity of a bubble, relative to the water velocity	m/s
ΔU	Difference between U_1 and U_2	m/s
v_i	velocity in direction i	m/s
v_m	Horizontal component of nth measurement	m/s
$v_{m,n}$	nth measurement of velocity in horizontal probe direction	m/s
v_K	Kolmogorov velocity scale	m/s
v_p	Velocity of a scattering particle	m/s
$v_{p\perp}$	Velocity perpendicular to the bisector of the incident laser beams	m/s
$v_{1,2,3}$	Velocities	m/s
V_{gas}	Volume of the total gas in the measuring section	m^3
x, y, z	Coordinates	m

$x_{1,2,3}$	Coordinates	m
X_g	Phase discriminator	-
$y_{1/2}$	y-position where U equals U_m	m
y_i	ith measuring point in y-direction	m
z_j	jth measuring point in z-direction	m

Greek symbols

Symbol	Description	Dimension
α	1) Gas fraction	-
	2) Angle	$^\circ$
α_δ	Slope of edge of boundary layer	rad
β	Angle between particle direction and direction of observation	$^\circ$
γ	Angle between $v_{p_\perp}$ and v_p	$^\circ$
ϵ	Dissipation rate of turbulent kinetic energy	m^2/s^3
η_K	Kolmogorov length scale	m
$\theta, \theta_1, \theta_2$	Angle between particle direction and incident laser beam (1),(2)	$^\circ$
Θ	Half angle between incident laser beams	$^\circ$
κ	Von Karman constant	-
λ	1) Dimensionless velocity	-
	2) Wavelength	m
λ_L	Taylor micro length scale	m
λ_T	Taylor micro time scale	s
ν	1) Kinematic viscosity	m^2/s
	2) Mean data rate	$1/s$
ξ	Dimensionless position	-
ρ	Density	kg/m^3
$\rho(\tau)$	Autocorrelation function	-
σ	1) Standard deviation	m/s
	2) Surface tension	N/m
τ	1) Time parameter	s
	2) Lag time	s
τ_m	Maximum lag time	s
τ_{rise}	Time needed for bubble to cover probe tip	s
$\Delta\tau$	Sample time step	s
$\tau_{i,j}$	Reynolds stress tensor	kg/ms^2
τ_k	Slot around $k\Delta\tau$	s
τ_K	Kolmogorov time scale	s
Φ	1) Total water flow through section	m^3/s
	2) Total air flow through section	m^3/s
ϕ	Air flow through capillary	m^3/s

χ	Scaling factor	-
ω	vorticity vector	rad/s

Other

Symbol	Meaning
DACQ	Data Acquisition Unit
DFT	Discrete Fourier Transform
FIND	Flow information display (software)
IFA	Intelligent flow analyser
PMT	Photo multiplier tube
PSD	Power Spectral Density function
Re	Reynolds number
TBD	Time between data

Contents

Chapter 1

Introduction

1.1 Scope of the project

During the last years, quite some effort has been made to gain more insight in the behaviour of two phase flows. There are many over-all descriptions of these flows, but mostly they are experimentally derived, while the flow is seen as a 'black box', without detailed knowledge of the physical backgrounds. This approach is getting less interesting for academic investigations, because the increasing possibilities of numerical modelling make more detailed approaches possible.
For really understanding the physical phenomena of two phase flows (e.g. the mutual interaction between the phases, and the changes of flow characteristics) simple flow-situations have to be chosen for which the one-phase equivalent is well understood. In these simple situations, a second phase can be inserted, to get a two-phase flow, which is as basic as possible. In the past, research has been done on the influence of homogeneous distributed bubbles in a channel flow [Lance and Bataille, 1991].
The next step to a more complicated, and industrial situation, is the introduction of a shear in the mean velocity of the fluid phase. This situation is found in the planar bubbly mixing layer. It consists of two merging bubbly flows, each with its own velocity and gas fraction, forming a mixing layer. Because of the profound mutual interaction between the two phases, this situation is well suitable for investigating the basics of two phase flows.

1.2 Objectives of the project

The planar two phase mixing layer is investigated experimentally. Simulated data are available, so experimental results are needed for comparison with the simulations.
Before doing so, the setup has to be tested on the validity of the assumptions, as the homogeneous distribution of the bubbles, the flatness of the velocity profiles outside the mixing layers, the two-dimensionality of the profiles, and the spectral behaviour of the flow.
This thesis will mainly deal with these preliminary investigations, and gives a description of the setup and its properties, including tests of the single phase situation.

1.3 Structure of the thesis

The theoretical aspects of one and two phase mixing layers will be explained in Chapter 2, as well as aspects of turbulence, and signal processing. Chapter 3 describes the used measuring methods, while Chapter 4 gives an overview of the experimental setup. The results are shown and discussed in Chapter 5, while the recommendations for future research are given in Chapter 6. In Chapter 7, the conclusions of the investigations are given.

Chapter 2

Theory

2.1 Introduction

A mixing layer consists of two cocurrent flows with different properties, merging after a certain position. These different properties can consist of difference in temperature, density, velocity or gas fraction. In this study, the case concerning a difference in velocity is considered. Difference in gas fraction will be investigated in the future. This situation is shown in Figure 2.1. The velocities of the two flows are U_1 and U_2 respectively, with a difference of $\Delta U = U_1 - U_2$. This velocity-difference (what also can be interpreted as a difference in momentum) shall spread out, because the shear stress at the separating boundary of the two flows, will bring about the exchange of momentum. So the high velocity will decrease, by loss of momentum, and the low velocity will increase with a same amount. The mutual influences are restricted to a certain part of the flow. This region, called the mixing zone, is spreading in the flow direction. To give a good description of this situation, the flow can be divided in three zones: one with an undisturbed velocity of U_1, one with an undisturbed velocity of U_2, and the third zone consisting of a layer between these two undisturbed layers. The mean velocity in this layer increases monotonic from the low to the high velocity. In this study, the planar mixing layer is examined. This means that a two dimensional situation is assumed, with no dependency in the depth direction. Also the influences of the boundaries of the measuring section are excluded by measuring at positions, which are far enough from all walls.

2.2 Definition of used quantities

Coordinates To describe the mixing layer, the following coordinate-system is introduced, also shown in Figure 2.1. The vertical direction is denoted by x or x_1, the horizontal direction by y or x_2, while z (or x_3) is the direction perpendicular to x and y.

Velocities The velocity in x-direction is written as u, or as v_1, the velocity in y-direction as v or v_2, and in z-direction as w or v_3. For convenience, U is often used for

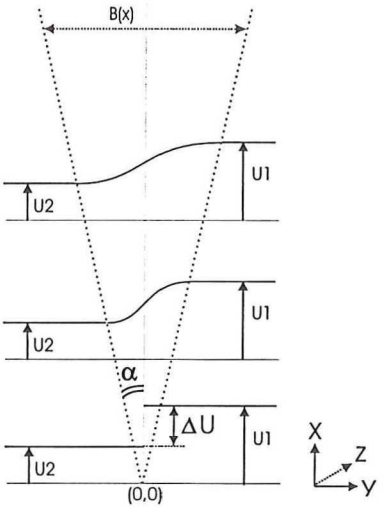

Figure 2.1: Schematic overview of a mixing layer

the mean velocity in the main (vertical) direction.

Gas fraction If also air bubbles are included, the gas-fraction α, also called hold-up, is defined as the ratio of the gas volume to the total volume:

$$\alpha = \frac{V_{gas}}{V_{tot}} \tag{2.1}$$

This equation gives an overall-description of the gas-fraction. If we are interested in the local gas-fraction, it can be defined as the time a certain position is in air, related to the total time:

$$\alpha(x, y, z) = \frac{1}{T} \int_T X_g(t)\, dt \tag{2.2}$$

with

$$X_g(t) = \begin{cases} 0 & \text{if (x,y,z) is in water,} \\ 1 & \text{if (x,y,z) is in gas.} \end{cases}$$

and T the measuring time.

2.3 Dimensionless description

An important characteristic of a mixing layer is the possibility of a self-similar description. The assumption of conservation of momentum leads (via dimension analysis, see Van den Akker [1997]) to a linear relation between the width B of the mixing layer and the height x:

$$B = \alpha x \tag{2.3}$$

where α is called the spreading rate. Its value amounts usually $\pm$ 5 % [Roig, 1993]. By comparing the position y with the width B, or (which is the same, according to equation 2.3) with the height x, and the relative velocity difference $(U(x, y) - U_2)$ with

the total difference ΔU, a description of the velocity-profile can be given, which is *only* a function of the dimensionless position ξ:

$$\frac{U(x,y) - U_2}{\Delta U} = f(\xi) \tag{2.4}$$

$$\xi = \frac{\chi(y - y_{1/2})}{x} \tag{2.5}$$

with $y_{1/2}$ the position where the velocity equals the mean of U_1 and U_2:

$$y_{1/2} = y(U = U_m = \frac{U_1 + U_2}{2}) \tag{2.6}$$

and χ a scaling factor, which can estimated as [Roig, 1993, page 96]:

$$\chi = \frac{\chi_0}{\lambda} \tag{2.7}$$

where χ_0 must be derived experimentally, and λ is a dimensionless velocity, defined as:

$$\lambda = \frac{\Delta U}{2U_m} = \frac{U_1 - U_2}{U_1 + U_2} \tag{2.8}$$

(As the increase of the width essentially depends on time, the $(U_1 + U_2)$-factor in λ can be seen as a transformation from time to position, while ΔU describes the dependency of the spreading rate α on the velocity difference.)
The choice for the function $f(\xi)$ can not be derived exactly in a analytical way. However, we assume $\lim_{\xi \to -\infty} f(\xi) = 0$, and $\lim_{\xi \to \infty} f(\xi) = 1$. If we suppose penetration theory for the exchange of momentum, for a cocurrent traveller, we find the following function, proposed by Görtler [Roig, 1993]:

$$f(\xi) = \frac{1}{2}\{1 + erf\ (\xi)\} \tag{2.9}$$

where $erf\ (\xi)$ stands for:

$$erf(\xi) = \frac{2}{\sqrt{\pi}} \int_0^{\xi} e^{-z^2} dz \tag{2.10}$$

For $y_{1/2}$ a linear relation with height is expected [Roig, 1993].
The dimensionless description gives the possibility to qualify the mixing layer, because of the unique representation of the velocity profiles. A more comprehensive description can be found in Tennekes and Lumley [1972].

2.4 Turbulence

Globally, two different flow regimes can be distinguished: laminar and turbulent flow. The most important parameter to distinguish between these two regimes is the Reynolds number. This dimensionless number is defined as the ratio between inertia forces and viscous forces in a flow:

$$Re = \frac{U\ x}{\nu} \tag{2.11}$$

where ν, U and x are respectively the kinematic viscosity [m^2/s], the mean velocity in the flow [m/s] and a characteristic dimension of the flow [m]. Laminar flow is

characterised by a relatively low Re-number, and turbulent flow by a high Re-number ($> 10^5$). In the same way, the Re-number of the mixing layer can be defined:

$$Re = \frac{\Delta U \; B(x)}{\nu} \tag{2.12}$$

with ΔU the difference in velocity between the two flows, and $B(x)$ the width of the mixing layer (see Section 2.3).

While a laminar flow has a predictable character, turbulent flow behaves chaotic. An important characteristic of turbulent flow is the existence of vortices. These vortices play an important role in spreading the existing gradients in the flow.

To be able to deal with turbulent flows, we start with the fundamental equations of motion, the so-called Navier-Stokes equation, and the continuity equation. For an incompressible Newtonian fluid, they are as follows:

$$\frac{\partial v_i}{\partial t} + v_j \frac{\partial v_i}{\partial x_j} = \frac{1}{\rho} \frac{\partial p}{\partial x_i} + \nu \frac{\partial^2 v_i}{\partial x_j^2} \tag{2.13}$$

$$\frac{\partial v_i}{\partial x_i} = 0 \tag{2.14}$$

In the first equation p represents the pressure [kg/ms^2] (where the influence of gravity is included into this term), v_i is the instantaneous velocity component in the i-direction [m/s] and x_i is the position in the i-direction. Equations 2.13 and 2.14 are based on the laws of conservation of momentum and mass respectively. Note that in these equations the Einstein summation convention has been used, which means that the terms of the equation should be summed over the repeated indices.

Because of the non-linear terms in the Navier-Stokes equations, integration is generally not possible. To deal with these equations in case of a turbulent flow, all quantities are separated in two contributions: one mean component, and one fluctuating part. This so-called Reynolds decomposition is explained for the velocity-term, but holds also for the pressure term in equation 2.13:

$$v_i = \overline{v_i} + v_i' \tag{2.15}$$

where $\overline{v_i}$ stands for the ensemble average of v_i, and v_i' for the fluctuating part. The mean of v_i' is by definition equal to zero.

In practise, $\overline{v_i}$ is calculated by a time average [Nieuwstadt, 1992]:

$$\overline{v_i}^T(t) = \frac{1}{T} \int_{-\frac{T}{2}}^{\frac{T}{2}} v_i(t+\tau) \; d\tau \tag{2.16}$$

with T the measuring time. The relation between the time average and the ensemble average is given by the ergodic principle:

$$\lim_{T \to \infty} \overline{v_i}^T = \overline{v_i} \tag{2.17}$$

The standard deviation σ (i.e. the root of the variance) is defined as:

$$\sigma_i = \sqrt{\overline{v_i'^2}} \tag{2.18}$$

Remark that in this equation, no Einstein summation should be applied.
By using the decomposition of equation 2.15 in equation 2.13, and averaging the whole equation, the following equation for the mean flow is obtained:

$$\frac{\partial \overline{v_i}}{\partial t} + \frac{\partial \overline{v_i v_j}}{\partial x_j} = -\frac{1}{\rho}\frac{\partial \overline{p}}{\partial x_i} + \nu \frac{\partial^2 \overline{v_i}}{\partial x_j^2} + \frac{\partial \overline{v_i' v_j'}}{\partial x_j} \tag{2.19}$$

Although equation 2.19 contains only mean-quantities, the last term is the mean of a product of fluctuating velocities. This introduces six extra (unknown) terms in the equation, so a closure-hypotheses is needed, before the equation can be solved.
The term $\rho\overline{v_i' v_j'}$ can be interpreted as the transport in the j-direction of momentum per mass in the i-direction by turbulent velocity fluctuations. This so-called Reynolds stress tensor:

$$\tau_{ij} = -\rho\overline{v_i' v_j'} \tag{2.20}$$

derives its name from its similarity to the molecular stress. Because the influence of the 'turbulent' shear stress is much bigger than the molecular stress, the Reynolds stresses play an important role in understanding the behaviour of mixing layers, and of turbulence in general [Nieuwstadt, 1992].
Besides the Reynolds stress tensor, several other characteristic quantities can be defined.
The *turbulence intensity* I is defined as the ratio of the fluctuation to the mean velocity:

$$I = \left(\frac{\overline{v_i'^2}}{\overline{v_i}^2}\right)^{\frac{1}{2}} * 100\% \tag{2.21}$$

Here Einstein summation has to be used. The vertical component of the turbulence intensity can be defined as:

$$I_x = \left(\frac{\overline{u'^2}}{U^2}\right)^{\frac{1}{2}} * 100\% \tag{2.22}$$

The same can be done for the y and z component.
The *Kolmogorov scales* are typical quantities for the dimension of the smallest vortices in a flow, their lifetime and velocity respectively:

$$\eta_K = (\frac{\nu^3}{\epsilon})^{\frac{1}{4}} \tag{2.23}$$

$$\tau_K = (\frac{\nu}{\epsilon})^{\frac{1}{2}} \tag{2.24}$$

$$v_K = (\nu\epsilon)^{\frac{1}{4}} \tag{2.25}$$

Here η_K is the Kolmogorov length [m], τ_K the time [s] and v_K the velocity [m/s], ν the dynamic viscosity [m/s^2], and ϵ the energy dissipation rate [m^2/s^3].
ϵ can by estimated as the ratio between the amount of energy in the biggest possible eddy, and the lifetime of that eddy L/U:

$$\epsilon \approx \frac{U^2}{L/U} = \frac{U^3}{L} \tag{2.26}$$

Here, U and L are the characteristic velocity and length scale. Equation 2.26 can also be used with ΔU and B instead of U and L, giving the Reynolds number for the mixing layer. A more precise estimate can be obtained by considering the amount of energy dissipation per mass for pipe flow:

$$\frac{\Delta p}{\rho} = 4f\frac{L}{D_h}\frac{1}{2}U^2 \tag{2.27}$$

with Δp the pressure drop [N/m^2] over a length L [m], D_h the hydraulic diameter [m], ρ the density [kg/m^3] and f the friction factor, being a function of the Re-number. The dissipation per second is found by multiplying with U/L:

$$\epsilon = 2f\frac{U^3}{D_h} \tag{2.28}$$

Besides the Kolmogorov scales, also the *Taylor scales* are often used, as a description for the micro scales. The Taylor micro time scale λ_T is defined by:

$$\overline{\left(\frac{\partial u'}{\partial t}\right)^2} = \frac{\overline{u'^2}}{\lambda_T^2} \tag{2.29}$$

The Taylor micro time scale is a measure for the transition from micro- to macro time scales. It is globally one order bigger than the Kolmogorov time scale.

In the same way the Taylor length scale λ_L can be defined by:

$$\overline{\left(\frac{\partial u'}{\partial x}\right)^2} = \frac{\overline{u'^2}}{\lambda_L^2} \tag{2.30}$$

The Taylor scales are often used (just as the Kolmogorov scales) for defining the turbulence. The Taylor micro time scale can be derived from the correlation function (see section 2.5), by using [Nieuwstadt, 1992, page 148]:

$$\overline{\left(\frac{\partial u'}{\partial x}\right)^2} = -\overline{u'^2}\frac{\partial^2 \rho(\tau)}{\partial \tau^2} \tag{2.31}$$

The Taylor micro length scale can be related to the time scale, by using the Taylor hypothesis [Nieuwstadt, 1992]:

$$\frac{\partial}{\partial t} \approx -U\frac{\partial}{\partial x} \tag{2.32}$$

It can be interpreted as an eddy moving by so rapidly through the measuring volume, that no appreciable change of the eddy can occur, i.e. as if it is frozen. This means that for the relation between λ_T and λ_L holds:

$$\lambda_L = U\lambda_T \tag{2.33}$$

Development of turbulent boundary layers According to Tennekes [1972], a turbulent boundary layer grows linearly with an angle α_δ [rad]:

$$\alpha_\delta \simeq \frac{0.28}{U/u_* - 1/\kappa} \tag{2.34}$$

with κ the von Karman constant (≈ 0.4). For the friction velocity u_* holds:

$$u_*^2 = -\frac{D_h}{2\rho}\frac{\Delta p}{L} \tag{2.35}$$

according to eq. 5.2.5 in Tennekes [1972]. Using equation 2.27 gives a value of $f\ U^2$ for u_*^2, with f the friction factor. This results in:

$$\alpha_\delta \simeq 0.022 \tag{2.36}$$

2.5 The correlation function and spectrum

Although a turbulent flow behaves chaotic, this doesn't mean that the movement of the flow is completely random; a correlation exists between the velocity at a certain moment, and the velocity some time later, measured at a fixed point. This correlation is expressed in the autocovariance, or autocorrelation function. The autocovariance function is defined as:

$$R(\tau) = \overline{u'(t)\ u'(t+\tau)} \tag{2.37}$$

having a separation or lag time τ. The autocovariance function is only a function of τ, and not of t, when dealing with a stationary process. When the autocovariance function is scaled with the value at $\tau = 0$ (being the variance of the signal), the autocorrelation function is obtained:

$$\rho(\tau) = \frac{R(\tau)}{R(0)} \tag{2.38}$$

Some important properties of this function are:

1) $\rho\ (0) = 1$
2) $|\rho(\tau)| \leq \rho(0) \quad \forall t$
3) $\rho(\tau) = \rho(-\tau)$
4) $\rho(\tau) \to 0$ as $\tau \to \infty$

The chaotic character of the flow comes back in the last property: no forecast of the flow can be made for large lag times.

The autocorrelation gives the possibility to define an integral time scale $\mathcal{T}$, defined as:

$$\mathcal{T} = \int_0^\infty \rho(\tau)\ d\tau \tag{2.39}$$

This time scale can be interpreted as a measure for the time separation for which correlation exists. It can be identified with the lifetime of the biggest eddies: L/U (see equation 2.26), or, as a more accurate relation [Tennekes and Lumley, 1972]:

$$\mathcal{T} \approx \frac{1}{3}\frac{L}{U} \tag{2.40}$$

Besides the time dependency of the signal, also the spectrum gives a lot of information about the flow properties. This frequency spectrum can be obtained by using the following equation:

$$S(\omega) = \mathcal{F}(u(t))\mathcal{F}^*(u(t)) \tag{2.41}$$

where $\mathcal{F}$ denotes the finite Fourier transform, and $\mathcal{F}^*$ its complex conjugated.
$S(\omega)$ is called the power spectral density function (PSD), because $S(\omega)d\omega$ gives the contribution to the total energy of the signal.

The PSD and the autocovariance are related by the Fourier transform:

$$S(\omega) = \frac{1}{2\pi} \int_{-\infty}^{\infty} e^{-i\omega\tau} \, R(\tau) \, d\tau \tag{2.42}$$

$$R(\tau) = \int_{-\infty}^{\infty} e^{i\omega\tau} \, S(\omega) \, d\omega \tag{2.43}$$

The normalised power spectral density function $h(\omega)$ is given by:

$$h(\omega) = \frac{S(\omega)}{\sigma^2} = \frac{1}{2\pi} \int_{-\infty}^{\infty} e^{-i\omega\tau} \, \rho(\tau) \, d\tau \tag{2.44}$$

In the equations above, ω [s^{-1}] can be related to the rotation speed of the eddies. This should be done with care, because the eddies are finite, while the Fourier transformation supposes (infinite) travelling waves. However, the small frequencies in the spectrum can be connected with the large (macro) scales, while the high frequencies represent the micro scale. The range between the macro and micro scale is called the inertial subrange. It is characterised by its non-dissipativity. This follows from the fact that at this scale, the Reynolds number is high, which means that dissipation by viscosity can be neglected. The energy is only transported from the big eddies to smaller ones by a cascade process of breaking up. At Kolmogorov scale, the viscosity gets its influence, and dissipates the energy. Calculation of the Reynolds number at this scale gives that it equals unity, which shows again that at this scale, the energy can by dissipated by viscosity.

From dimension analysis follows that the inertial subrange is characterised by [Nieuwstadt, 1992]:

$$S(\omega) \sim \omega^{-5/3} \tag{2.45}$$

For convenience, often the frequency f is used. It 's related to ω by $f = \omega/2\pi$.

The borders of the inertial subrange can globally be estimated as $f = U/L$ for the macro scale, and as $f_K = 1/\tau_K$ for the micro scale. Typical one and two phase turbulence spectrum, measured by Lance [1991], are depicted in Figure 2.2.

2.6 Statistics of discrete parameter processes

Time domain statistics The equations in the section above all deal with continuous signals. Because of the discrete character of the LDA measurement technique (see Section 3.1.1), discrete forms of the used quantities are required. The mean velocity in the x-direction is estimated as:

$$\hat{U} = \hat{\overline{u_1}} = \frac{1}{N} \sum_{n=1}^{N} u_n \tag{2.46}$$

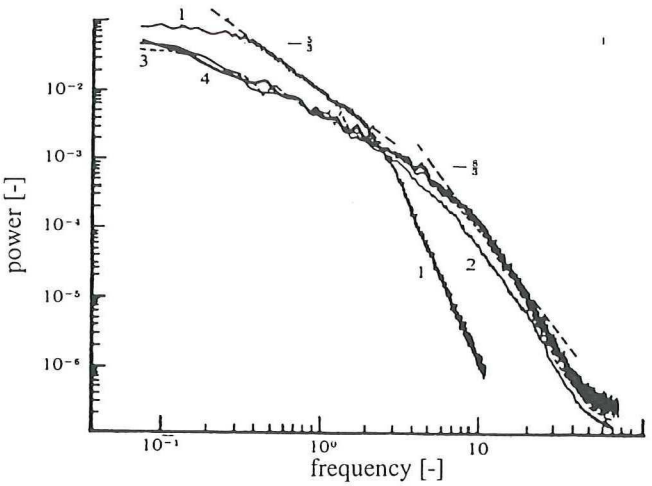

Figure 2.2: The spectra according to Lance, for one and two phase flow (1: one phase; 2,3,4: two phase)

where u_n is the n^{th} measurement in a series of N. The estimated standard deviation is given by:

$$\hat{\sigma} = \frac{1}{N-1}\sqrt{\sum_{n=1}^{N}(u_n - \hat{U})^2} \tag{2.47}$$

The estimated autocovariance function for a uniform sampled signal is:

$$\hat{R}(\tau) = \sum_{n=1}^{N-|\tau|}(u_n - \hat{U})(u_{n+|\tau|} - \hat{U}) \tag{2.48}$$

However, this estimation is not adequate for the randomly sampled LDA-signals. Several options exist to deal with this problem. One option is to resample the signal, using the sample and hold technique, or linear interpolation between successive measurements. From this resampled signal, both the autocorrelation function and the spectrum can be calculated.

Another method to calculate the autocorrelation function of a randomly sampled signal is called the slotting technique [Tummers and Passchier, 1996]. It estimates the autocorrelation function by the following algorithm:

$$\hat{R}(\tau_k) = \frac{sum\{(u_i - \hat{U})(u_j - \hat{U})\}(\tau_k)}{H(\tau_k)}, \quad k = 1, 2, M-1 \tag{2.49}$$

where $sum\{.\}(\tau_k)$ denotes the sum of all cross-products falling in the k^{th} slot and $H(\tau_k)$ is the number of cross-products within the k^{th} slot. The k^{th} slot is defined as:

$$\tau_k = (k - 1/2)\Delta t < \tau < (k + 1/2)\Delta t, \quad k = 0, 1, ..., M-1 \tag{2.50}$$

where Δt is the slot width. The integer M follows from $M = \tau_m/\Delta t$, with τ_m the maximum lag time.

Chosen is for resampling, and using linear interpolation. Linear interpolation is used, because this gives a better representation of the real signal then sample and hold does citeMaanen. However, as mentioned by Tummers and Passchier [1996], the data rate must be high enough to get good results.

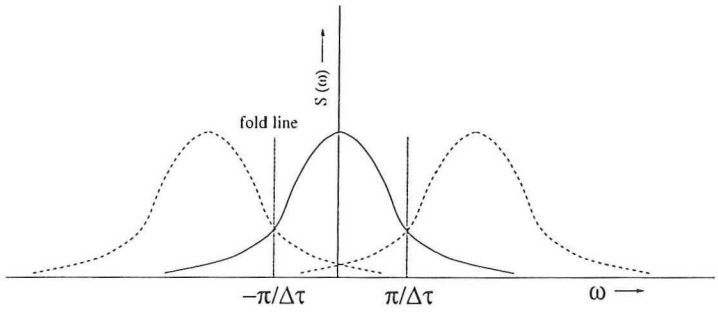

Figure 2.3: The aliasing effect

Frequency domain statistics With N numbers of independent input samples, no more than N frequencies in the spectrum can be calculated. The highest detectable frequency is determined by half the sample frequency in time domain. This can be understood by considering that each present sine wave requires at least two samples per wave length to be detected. This frequency is called the Nyquist frequency, and can be written as:

$$f_{Nyq} = \frac{1}{2\Delta\tau} \tag{2.51}$$

with $\Delta\tau$ the time step between two successive samples.
The N samples are distributed over the range $(-f_{Nyq}, f_{Nyq})$, thus the sample interval in frequency domain will be $\Delta f = 2f_{Nyq}/N$. This means that the PSD will be defined for:

$$f_n = \Delta f \; n = \frac{1}{\Delta\tau}\frac{n}{N}, \quad n = -\frac{N}{2}, -\frac{N+2}{2}, ..., \frac{N}{2} \tag{2.52}$$

To calculate the discrete PSD, the discrete Fourier transform (DFT) is used. This means that the Fourier coefficients $\{c_k\}$ are calculated via:

$$c_k = \sum_{i=0}^{N-1} u_n e^{2\pi jnk/N} \tag{2.53}$$

where c_k^2 is the contribution of frequency $k\Delta f$ to the total energy. The normalised spectrum can be found by dividing by $\sum c_k^2$.

Aliasing As mentioned in the section above, frequencies higher than f_{Nyq} are not directly detectable. However, these frequencies have their influence upon the spectrum. This can be seen from Figure 2.3. When a frequency is higher than f_{Nyq}, it is 'seen' as a frequency equal to $f_i + 2mf_{Nyq}$, (with $m \in \mathcal{Z}$). The frequency is 'folded' into the Nyquist range. To prevent disturbance in this way, the high frequencies are normally filtered out. In the case of LDA measurements, this is not possible because of the discrete character of the LDA technique. This means that the Nyquist frequency (and thus the mean data rate) should be so high, that the energy of the folded frequency is negligible compared to the original frequency.

Number of measurements and blocks Besides the resolution of the spectrum, also its accuracy is important. For the accuracy of the PSD, the following relation

holds [Van der Haagen, 1995]:

$$Var\ \{PSD(f)\} = E^2\{f\} \tag{2.54}$$

where $E\{f\}$ is the expected value of f. Thus the variance of the estimations equals 100 %. To decrease this variance, the signal can be divided into blocks, over which the PSD is averaged. As an indication for the variance of the PSD, being divided into m blocks, holds:

$$Var\ \{PSD(f)\} \approx \frac{1}{m}\ PSD^2(f) \tag{2.55}$$

By dividing the signal in m blocks (each having a time of T_{total}/m) the accuracy of the spectrum increases, while the resolution decreases, according to equation 2.52.

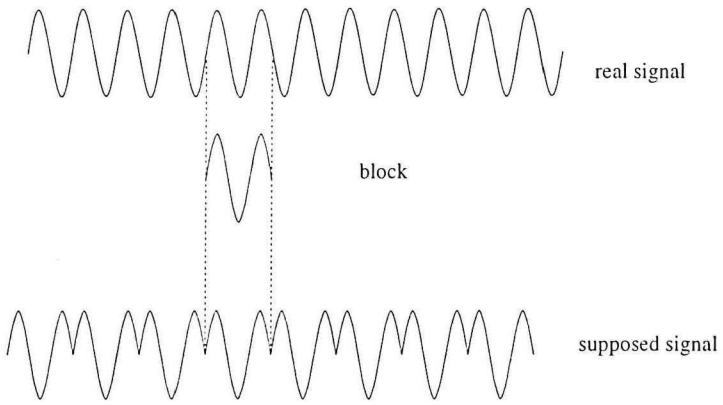

Figure 2.4: The leakage effect

Leakage and windowing A Fourier transform assumes an infinite signal. When measuring during a finite time, this block is repeated, and thus an infinite signal is formed (see Figure 2.4). This will give no problems when these blocks have the same value and slope for the start and the end of the block, but when they differ, many high frequencies are introduced.
To avoid this effect, a window is applied to the data, which presses the signal to zero at the boundaries of the block. For the investigations reported in this thesis, the Hanning filter is used:

$$H(k) = \frac{1}{2}\ (1 - cos(\frac{2\ \pi\ k}{N})) \tag{2.56}$$

Figure 2.6 shows the effect of the Hanning filter upon the signal.

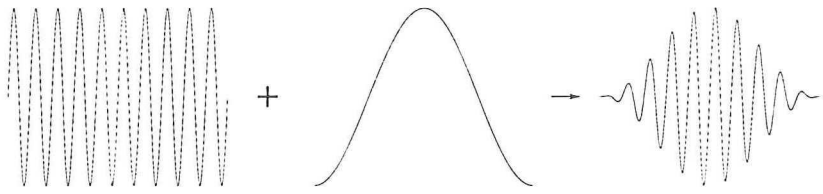

Figure 2.5: The effect of the Hanning filter

Zero padding When using the inverse Fourier transform of the spectrum to obtain the correlation function, two intertwined functions are summed: one the correlation function from $\tau = 0$ to $\tau = \mathrm{N}$, the other the correlation function from $\tau = \mathrm{N}$ to $\tau = 0$. The two can be separated by adding N zeroes to the original data, before it is Fourier transformed. This technique is called zero padding [Van der Haagen, 1995].
Another effect of zero padding is that the number of discrete frequencies in the spectrum is doubled, as the number of points is increased from N to 2N. Of course no new information is added, thus the newly obtained frequency points are combinations of already obtained points.
A more comprehensive description of spectral analysis can be found in Priestley [1975].

2.7 Principle of bubble formation

Poiseuille flow As will be mentioned in more detail in Section 4.1.2, the bubbles are formed by a sparger, consisting of many tubes, with a length of 25 mm, and an internal diameter of 1.0 mm.
The air is driven out of the tubes by the existence of a pressure drop over the tube. The magnitude of this drop depends on the velocity according to:

$$\Delta p = f \frac{SL}{A} \frac{1}{2} \rho v^2 \tag{2.57}$$

where f is the friction factor [-], S the circumference of the tube [m], L its length [m], A the surface of the cross-section [m^2], ρ the density of the air [kg/m^3]and v the mean velocity of the air in the tube [m/s]. For a round tube, and low Reynolds numbers, equation 2.57 can be rewritten to:

$$\Delta p = \frac{128\eta}{\pi D^4} L\phi \tag{2.58}$$

with ϕ the air flow through a tube. This equation is called the Poiseuille equation.
Used is the relation between f and Re (valid if $Re < 2 * 10^3$):

$$f = \frac{16}{Re} = \frac{16\ \eta}{\rho v D_h} \tag{2.59}$$

with D_h the hydraulic diameter. Although the number 16 is only valid for a round tube, it is used as an approximation for other situations. For the situation of Figure 2.6, with a wire of thickness D_1 in the tube, D_h in equation 2.58 must be replaced with $D_1 - D_2$, S with $\pi(D_1 + D_2)$ and A with $\pi(D_1^2 - D_2^2)$. This gives:

$$\Delta p = \frac{128\eta}{\pi} \frac{L\phi}{(D_2 + D_1)(D_1 - D_2)^3} \tag{2.60}$$

Comparing Equation 2.60 with 2.58 suggests the definition of an equivalent diameter D_0, being the diameter of a round tube resulting in the same pressure drop as a tube with a wire:

$$D_0^4 = (D_1 + D_2)(D_1 - D_2)^3 \tag{2.61}$$

Calculation shows that inserting a wire with diameter $D_1 = 0.7\ D_2$, results in a increase of the pressure drop with a factor 22. So the pressure drop is increased very effectively by the wires.

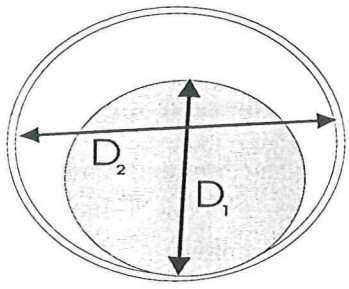

Figure 2.6: Intersection of the tube with wire

surface tension The effect of surface tension implies that a pressure drop exists over a curved surface, with a magnitude of:

$$\Delta p = \sigma \left(\frac{1}{R_1} + \frac{1}{R_2} \right) \tag{2.62}$$

where σ [N/m] is the surface tension, $\frac{1}{R_1}$ and $\frac{1}{R_2}$ the radii of the curves, describing the shape of the surface. When is assumed that the interface between the gas and the liquid phase consists of half a sphere, for both R_1 and R_2 the value of the radius of the tube can be chosen.

2.8 Two phase mixing

In the one phase case, the flow and its properties can be calculated easily in a numerical way, using an simple model (e.g. the k-ϵ model) [Nieuwstadt, 1992, page 125]. However, in two phase flow the properties of the mixing layer, and also their modelling, are strongly complicated. The most important reasons are:

- Because of the numerous inclusions, the assumptions of the turbulence models are no longer valid. All these inclusions have their own boundary conditions, and own trajectories. This makes it impossible to use the usual models any longer. So special attention has to be paid to the way of modelling the influence of the bubbles.
- A profound mutual influence exists between the two phases. The trajectories of the bubbles are (partly) influenced by the surrounding flow, while the flow is disturbed by the bubbles. In the experimental studied case, the Taylor length scale (equation 2.30) is expected to be of the same order of magnitude as the size of the bubbles [Lance and Bataille, 1991], which means that the turbulence 'feels' the presence of the bubbles, while the bubbles 'feel' the turbulence. This increases the complexity of the situation, while the influences can not be separated from each other, but have to be taken into account simultaneously. This effect is confirmed by studying the influence of the two phase flow upon the energy spectrum [Lance and Bataille, 1991]; while the big eddies are somewhat 'broken up' into smaller eddies by the presence of the bubbles, the total amount of smaller scales in the flow will increase, by the influence of the wakes of the bubbles (see

Figure 2.7). In this wake, small vortices are present, which will increase the total contribution of the high frequencies in the spectrum. As can be seen from Figure 2.2, the influence of the bubbles holds over the whole width of the spectrum.

- Another important contribution to the complexity of two phase flow, is the presence of so-called pseudo-turbulence. As can be seen from equation 2.21, the fluctuation of the velocity is normally connected with the turbulence of the flow. However, the (approximately helicoidal) trajectories of the bubbles, as well as the sideward flow of the water during the pass of a bubble, induce fluctuations of the fluid, which can not be contributed to turbulence. The same holds for the deformation of the bubbles when moving (Figure 2.7). A priori it is not known which part of the fluctuations is caused by 'real', and which part by pseudo-turbulence. Supposing helicoidal potential flow of elliptical-shaped bubbles, an estimate of the amount of pseudo-turbulence has been made by Lance and Bataille [1991].

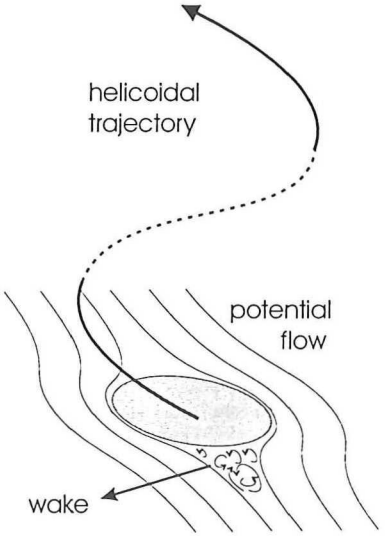

Figure 2.7: Helicoidal flow of a single bubble with a wake

The above mentioned items have their influence upon the macroscopic behaviour of the mixing layer.

The *spreading rate* α is expected to increase, since the exchange of momentum is stimulated by the movement of the bubbles. This can be explained by considering that in two phase flow, the momentum is transferred convective by the flow around the bubble, while in one phase flow, the momentum has to be transported by (turbulent) diffusion. So the presence of bubbles will increase the exchange-rate of momentum.

The estimation of the amount of *pseudo-turbulence* can, in its most simple situation, be seen as an excess of turbulence, compared with the one-phase situation. As mentioned above, this is not the situation in reality, but it can be useful to determine the order of magnitude of this effect. From literature [Lance and Bataille, 1991] appears, that for low gas fraction, and for pure water (where the wakes of the bubbles are very small), this approximation holds quite well. For bigger gas fractions (i.e. > 1 %) the mutual influence is too big, to justify this approximation.

The influence of the wakes can be estimated by [Lance and Bataille, 1991]:

$$\frac{u'_w}{l_w} \sim (\alpha/D) C_D U_R^3 \tag{2.63}$$

where u'_w is the fluctuating velocity induced by the wake, l_w the length scale associated with the dissipation of these fluctuations, C_D the drag coefficient, and U_R the velocity of the bubbles relative to the mean liquid velocity.

Chapter 3

Measuring Methods

3.1 Laser Doppler Anemometry

3.1.1 Measuring principle

Laser Doppler Anemometry (LDA) is a method for measuring accurately the velocity in a flow, without disturbance. The principle of this measuring technique is explained in the sections below.

Doppler shift The Laser Doppler Anemometry measuring method is based on the frequency shift of light scattered by a moving particle, compared with the frequency of the source. This effect is well known under the name 'Doppler effect'.

The Doppler shift, in the case of fixed source and observer, can be written as:

$$f_s - f_0 = \frac{f_0 v_p}{c}(\cos\theta + \cos\beta) \tag{3.1}$$

where f_s is the frequency [Hz] of the scattered light seen by the observer, f_0 the frequency of the light emitted by the source, c the speed [m/s] of light and v_p the velocity of the particle; θ is the angle [°] between the incident laser beam and the direction of the velocity of the scattering particle, and β the angle between the direction of the scattered light and the direction of the particle-velocity (see also Figure 3.1). Equation

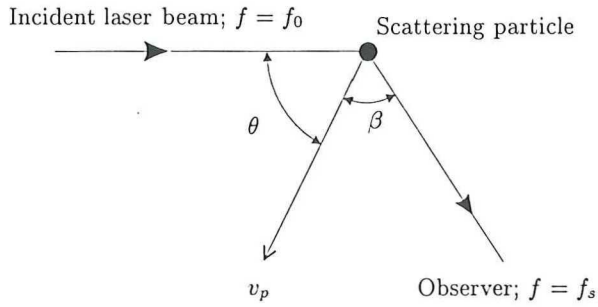

Figure 3.1: The orientation of the incident and scattered laser light relative to a moving scattering particle.

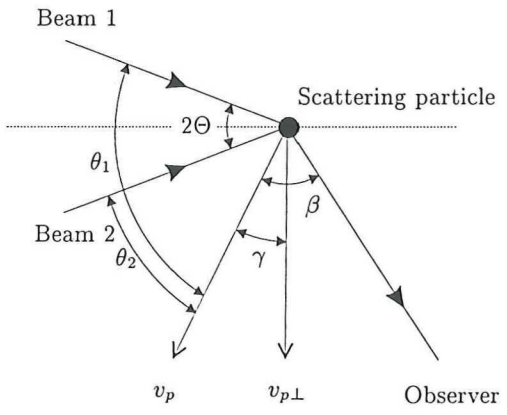

Figure 3.2: Orientation of illuminating beams and scattered light in the dual beam technique.

3.1 is only valid if the speed of the particle is much smaller than that of light.

Dual Beam method Because the velocity of the particle is much smaller than the speed of light, the Doppler shift will be very small, compared with the frequency of the laser light. It is not possible to detect the Doppler shift directly, because the frequencies are too high for direct detection. However, the difference in frequency of two signals can be determined by using optical beating. This means that two signals, with slightly different frequencies, are added and passed through a non-linear (e.g. a square-law) detector. The output contains a frequency, equal to the difference of both frequencies. Optical beating can be applied in LDA by using the dual beam method (see Figure 3.2). In this method, two incident laser beams are used, with a mutual angle of 2Θ. These two beams are obtained by splitting a beam into two beams, and let them intersect by using a lens. Because the angle between the incident beam and the direction of the particle velocity is different for both beams, they undergo a different Doppler shift. The difference between these shifts, called the beat frequency f_D [Hz], is characteristic for the velocity of the particle in the flow. For this frequency can be written:

$$f_D = f_{s,1} - f_{s,2} = \frac{f_0 v_p}{c}(cos\ \theta_1 - cos\ \theta_2) \tag{3.2}$$

The quantities used are depicted in Figure 3.2.

Substituting $\gamma = \frac{1}{2}(\theta_1 + \theta_2 - 180)$ [°] and $\Theta = \frac{1}{2}(\theta_1 - \theta_2)$ [°] gives:

$$f_D = \frac{2 v_p \cos\gamma\ \sin\Theta}{\lambda} \tag{3.3}$$

where λ is the wavelength [m] of the incident laser beams. In this equation the velocity perpendicular to the bisector of the two laser beams $v_{p\perp}$ can be introduced:

$$f_D = \frac{2 v_{p\perp} sin\Theta}{\lambda} \tag{3.4}$$

From this, it can be concluded that the observed frequency is independent of the angle of detection β.

Fringe method Another interpretation of the measuring principle of LDA is called the fringe method. The principle is shown in Figure 3.3. The intersection area of two

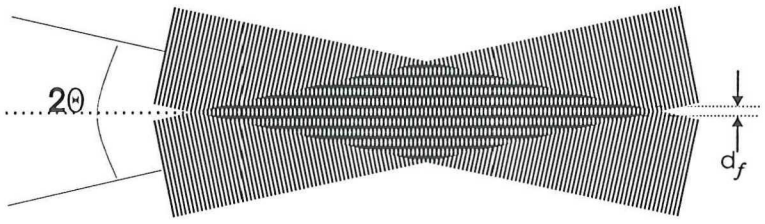

Figure 3.3: Fringe pattern as a result of superposition of two mutually coherent laser beams.

mutually coherent laser beams shows an interference area, consisting of a pattern of light and dark planes, parallel to the bisector between both illuminating laser beams. The distance between two dark planes can be calculated:

$$d_f = \frac{\lambda}{2 \sin \Theta} \tag{3.5}$$

A particle crossing the intersection plane will thus scatter light with a varying intensity, depending on the velocity of the particle (see Figure 3.4). The frequency of this intensity is:

$$f_D = \frac{v_{p\perp}}{d_f} = \frac{2 v_{p\perp} \sin \Theta}{\lambda} \tag{3.6}$$

So the frequency shift, calculated with the fringe method equals that using optical beating. The application of the fringe model should be used with care, because this pattern doesn't exist physically, but is only a 'pattern' detected by a square-law detector, like a photo multiplier or the human eye. (So actually, the pattern is not formed in the flow, but at the detector.) The exponential decay of the amplitude of the Doppler signal in

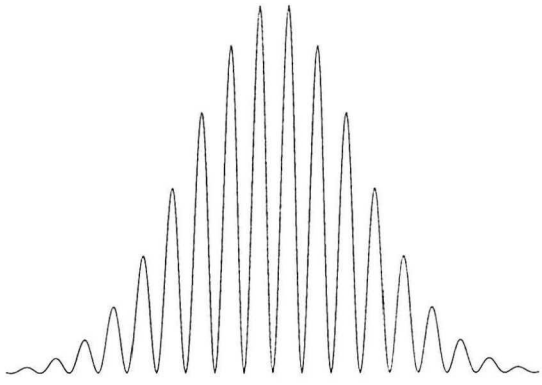

Figure 3.4: A typical Doppler burst signal after filtering

Figure 3.4 comes from the exponential distribution of the light intensity in the incident beams [Absil, 1995].

Preshift By the described method, the magnitude of the velocity vector perpendicular to the bisector of the two beams can be measured, but no discrimination of the direction can be made.
To overcome this problem, a frequency shift (called the preshift f_{shift} [Hz]) can be added to one of the incident beams. This causes a beat frequency equal to:

$$f'_D = f_{shift} + \frac{2v_{p\perp} sin\Theta}{\lambda} \tag{3.7}$$

The preshift causes the fringe pattern to 'move' into one direction. A particle with velocity zero will thus generate a frequency equal to the preshift, while negative velocities produce a Doppler shift smaller than the preshift. After subtracting the preshift, distinction is made between positive and negative velocities. The magnitude of the preshift has to be larger than the frequency corresponding with the largest expected negative velocity.

Multicomponent measurements Via a pair of laser beams, the velocity component perpendicular to the bisector of both beams can be measured. By using three pairs of laser beams, all intersecting at one point, the three components of the velocity can be measured simultaneously. This gives the possibility to measure correlations between different velocity components, such as the Reynolds stresses (see equation 2.20) directly. Difficulties are involved by placing all measuring volumes at exactly the same position [Doelman, 1997]. Also the assumption that a particle is determined by all three photo multipliers is not real in many cases. This decreases the amount of determinated particles, the data rate, drastically.
In this study, only 1-D and 2-D measurements are done.

Measuring volume The position where the velocity is measured is determined by the intersection area of the laser beams. The diameter d_0 [m] of the beams at the intersection position can be calculated [Guenter, 1990]:

$$d_0 = \sqrt{n_w}\left(\frac{4\lambda F}{\pi D_0}\right) \tag{3.8}$$

where n_w is the refractive index of the fluid, λ the wavelength of the beams in the fluid, F the focal distance of the probe lens, and D_0 the diameter of the beams just in front of the lens. The diameter of a laser beam is defined as the distance between the points where the intensity equals e^{-2} times the maximum intensity in the centre of the beam. The ellipsoidal shape of the overlap region has the following dimensions:
length of short axis (d_m): $d_m = d_0/\cos\Theta \approx d_0$
length of long axis (l_m): $l_m = d_0/\sin\Theta \approx d_0/\tan\Theta$

These approximations are only valid if 2Θ, the angle between the two incident beams, is small.

Seeding To do a velocity measurement, the LDA technique requires scattering of light. This can be caused by contaminations present in the flow, or by added particles, called seeding. The data rate, defined as the amount of measurements per second,

depends on the concentration of scattering particles in the flow. As a rule of thumb, one particle per measuring volume should be chosen. If there are less particles, the data rate is lower than possible, while if there are more, wrong frequencies are determined because of the interference of scattered light from different particles. Other conditions for the scattering particles are their size, mass and density. If they are too heavy, they don't follow the flow, and are not representable for the fluid flow. They also need to have the same density as the fluid, to get a good distribution of them in the flow, and prevent deposition of the seeding. Too big particles, i.e. bigger than the fringe distance (equation 3.5) give also bad results, since they always have a part illuminated, which makes it difficult to determine the velocity.

In this project, no seeding has been used, because of the big amount of (expensive!) seeding, needed for the whole setup. This means that the data rate is quite low, which gives problems with determination of the spectrum.

3.1.2 Error sources

The amount of particles moving through the measuring volume, depends on the velocity of the flow. This means that in the measuring volume, more often particles with a high velocity are detected, than slow-moving particles. This causes the so-called *velocity bias*: Not the time average, but an arithmetic average is calculated, which differs from the 'real' mean.
This bias source can be corrected by weighting the individual velocity with the absolute velocity:

$$U = \frac{\sum_{n=1}^{N} u_n / \sqrt{u_n^2 + v_n^2}}{\sum_{n=1}^{N} 1 / \sqrt{u_n^2 + v_n^2}} \tag{3.9}$$

Another correction method uses the transit time of the particle. This is based on the relation between the velocity of a particle, and the time it needs to pass the measuring volume:

$$U = \frac{\sum_{n=1}^{N} u_n \, \Delta\tau_n}{\sum_{n=1}^{N} \Delta\tau_n} \tag{3.10}$$

with $\Delta\tau_n$ the residence time for the n^{th} particle.
Another error source is called *amplitude bias*. Slow moving particles have more time for reflecting light, and thus have a higher probability to be detected. This tends the calculated velocity to a value beneath the real average.
A third error source (called *gradient bias*) is caused by the finite dimensions of the measuring volume. In theory, point measurements should be performed, while in reality, the velocity is averaged over the dimensions of the measuring volume. This can give wrong (mean and fluctuating) velocities when a gradient is present over the measuring volume.
For a more comprehensive description of error sources, see e.g. Absil [1995].

3.1.3 Inter-particle arrival time distribution

Scattering particles are assumed to be randomly distributed in the liquid. In this case, the arrival time to the measuring volume between successive particles is Poisson

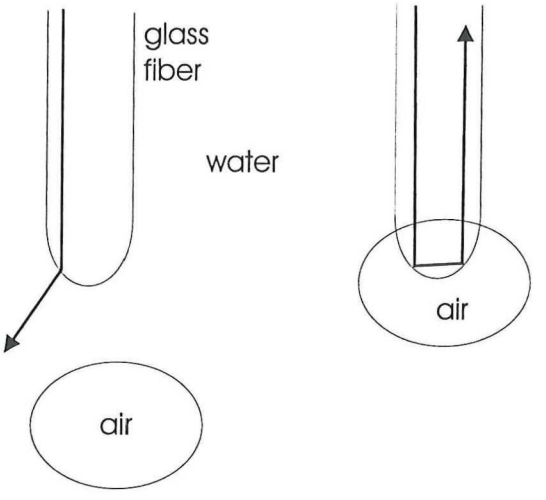

Figure 3.5: The different environments of the probe tip, resulting in a leaving or reflecting beam.

distributed. This means that the probability of finding a time interval Δt between two successive arrivals, denoted as the inter-particle arrival time, can be written as

$$p(\Delta t) = \nu \; e^{-\nu \Delta t} \tag{3.11}$$

where ν is the mean data rate being the ratio between the total amount of measurements and the total time.
The Poisson distribution supposes a linear relation between the logarithm of the probability density function (3.11) and the time between data $\Delta\tau$ (also called TBD).

3.2 Glass fibre probes

3.2.1 Measuring principle

The principle of the glass fibre probe measuring technique lays in the difference of refractive index of gas and liquid. A light signal is sent into a glass fibre, with a spherical shaped tip (see Figure 3.5). Depending on the refractive index of the surrounding, the light signal will leave the fibre (when the tip is in water, because of the almost equal refractive indices of water and glass) or reflect, when the tip is surrounded by gas. This gives the possibility to determine the time-dependent environment of the probe tip. In theory, two levels of the reflected signal can be distinguished: a high level for gas-surrounding situation, a low level for water around the tip, resulting in consecutive block shape (Figure 3.6). Each block represents one bubble.
The hold up at the position of the fibre tip can be calculated by:

$$\alpha = \frac{T_{gas}}{T_{total}} \tag{3.12}$$

with T_{gas} the time that the probe tip is surrounded with gas, and T_{total} the total measuring time.

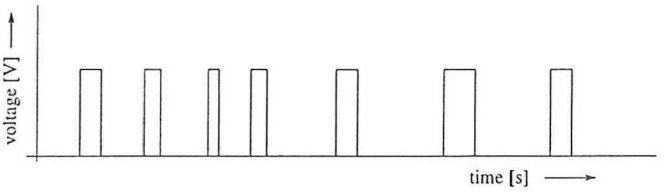

Figure 3.6: Theoretical signal from the fibre probe.

3.2.2 Bubble velocity and size determination

In the practical situation, several difficulties appear. The reflected signal is not of a block-shape, but is characterised by a shape as shown in Figure 3.7. The intersection time T is defined as the point where the signal goes from 10 % of the difference, to 90 %. This gives a small underestimate of the gas fraction determination. Another difficulty is that not all bubbles are detected. Small bubbles (i.e. of the size of the glass fibre) are not detected, but bounce off. Also bubbles, touching the tip at their side, are not detected. This gives an underestimate of the gas fraction of ± 10 % [Mulder, 1996].

Besides the gas fraction, other information can be obtained from the signal. Because

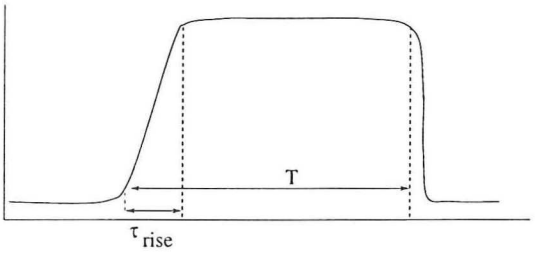

Figure 3.7: A typical shape of the voltage, corresponding to the pass of a bubble

of the finite dimension of the probe tip, it takes some time before the rising bubbles has totally covered the probe tip. This results in an certain time, before the maximal light quantity is reflected. From this rise time τ_{rise} [s], a rise velocity can be estimated by defining a reference length L_{ref} [m], which can be connected to the dimensions of probe tip [Cartellier, 1990]:

$$\tau_{rise} = \frac{L_{ref}}{v} \tag{3.13}$$

where v is the velocity of the rising bubble.

If the velocity of the rising bubble is known, it can be used to determine the intersection length of the bubble L_i, being equal to v/T, where T is the intersection time. If we assume spherical bubbles moving in line with the fibre, which are intersected at random positions, the diameter of the bubbles is:

$$D_{mean} = \frac{3}{2} L_{i,mean} \tag{3.14}$$

with $L_{i,mean}$ the intersection length, averaged over many bubbles.
The assumption of spherical bubbles is realistic if the diameter is smaller than 2 mm. In

other cases, an ellipsoidal shape can be assumed [Janssen and Warmoeskerken, 1991, page 93]. Remind that the factor 3/2 in equation 3.14 is only valid for spheres.

Estimation of rise velocity The gas fraction can be seen as the ratio of the supplied air to the rise velocity multiplied with the dimensions of the section:

$$\alpha = \frac{\Phi}{L\ B\ v_{rise}} \tag{3.15}$$

where Φ is the supplied air [m^3/s], L and B the length resp. the depth of the measuring section [m], and v_{rise} the velocity of the bubbles [m/s]. This velocity depends on the gas fraction [Van den Akker, 1997], but a simple estimate for low gas fractions is:

$$v_{rise} \approx U + v_{\infty} \tag{3.16}$$

where v_{∞} is the velocity of a single bubble in a infinite, stagnant fluid. However, this velocity depends on the size of the bubbles [Janssen and Warmoeskerken, 1991, page 80], but mostly its value is somewhere between 0.25 and 0.3 m/s [Janssen and Warmoeskerken, 1991, page 94].
In this way an approximation can be made for the relation between the supplied air and the mean hold up.

3.3 LDA in two phase flow

Although no two phase measurement are performed in this project, a short summary of the difficulties of two phase measuring are mentioned.

- The laser beams can be interrupted by passing bubbles. If one of the beams is interrupted before the intersection position, the measuring volume will vanish. This is also the case when a bubble moves through the intersection point. In these cases, no velocity can be determined, except for very special conditions. When a bubble interrupts the beam after the intersection place, a velocity can be measured, but it might be contaminated by the reflection from the bubble, and indirect reflections via other bubbles [Marié, 1983].

- It 's not clear which velocity is determined when a bubble moves through the measuring volume. Besides the water velocity, also the bubble velocity could be the measured quantity [Sheng and Irons, 1991].

- The data rate will decrease drastically by the interruption of the laser beams. Determination of statistical quantities is complicated by this fact. This means in practise frequency-depending quantities are difficult to be determined.

- A criterium is needed to distinguish between the fluid and gas phase. In literature, different options are found, but they all use the difference in intensity of reflected light by a particle and by a bubble. The intensity of the light reflected via a bubble is most times much higher than that of a seeding particle. Marié [1983] uses different photo multiplier supplies, to measure either the fluid or the

bubble velocity. Theofanous and Sullivan [1982] use a threshold level, resulting in neglecting the contribution of the bubbles, while Ellingsen and Roig [1997] remark to have no appropriate phase discrimination method at all.

Chapter 4

Experimental Setup

4.1 Global description

For experimental investigations, the setup described below, is built. A global overview of the setup is given is Figure 4.1. It consists of two separated water flows, individually

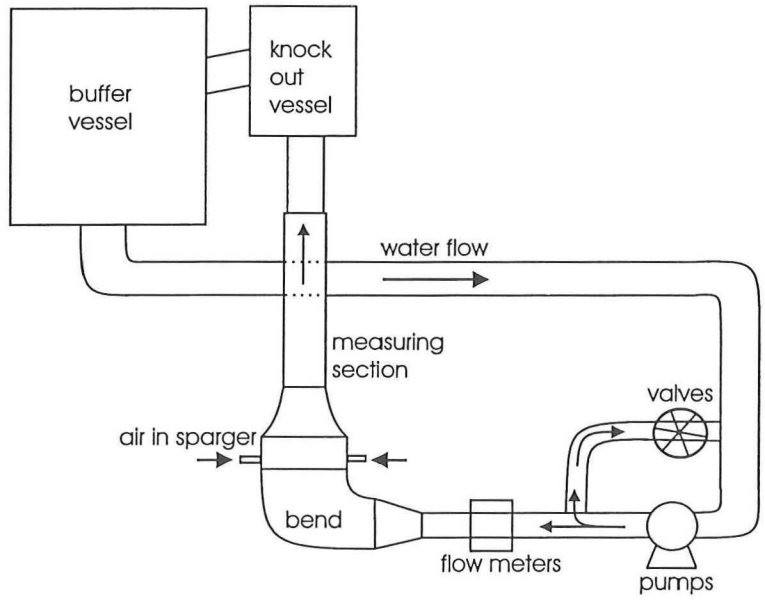

Figure 4.1: Global view of the experimental setup

driven by a pump. These flows merge in the measuring section. Air is supplied by a sparger. It leaves the flow in the knock-out vessel, while the water ends up in the buffer tank. From this tank (with a volume of 10 m^3) the flow returns to the pumps again. The different units of the setup are described in the following sections.

4.1.1 Water flow

The water flows are driven by two pumps, type NOWA 8020/185 AB.CDN.OB.2, with a capacity of 100 m^3/h, a power of 4 kW and a (constant) revolution-number of 1450

min^{-1}.
These pumps give a constant flow, while the flow in the measuring section can be adjusted by a bypass-loop (see Figure 4.1). By regulating the valve, placed in this loop, the amount of liquid flowing through the by-pass, and thus also the flow through the measuring section, can by regulated.
The velocities in the measuring section can be chosen between 0.5 and 0.85 m/s. The water flow is measured by Krohne Altometers, types IFS4000 and K300. For technical data is referred to Appendix B.

Bend To bring the flow from horizontal to vertical direction without creating much turbulence or secondary motion, special attention is paid to the bend. Several fins, with a mutual distance of 5 cm, are brought in, to lead the flow as much as possible, and to minimise secondary flow (see Figure 4.2). This part is constructed of aluminium.

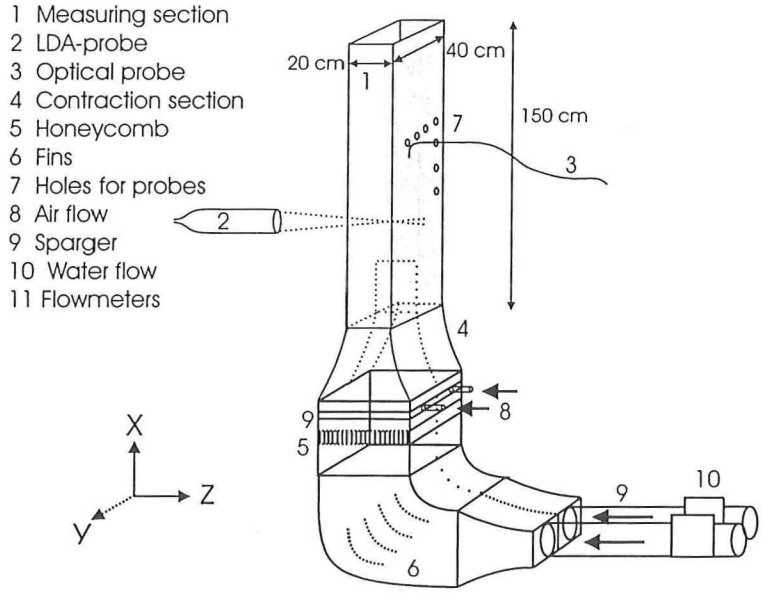

Figure 4.2: Measuring section and bend

Measuring Section The front side and both side walls of the measuring section are made of float glass, with a thickness of 19 mm, while the back is made of stainless steel (thickness 20 mm). The walls of glass offer the possibility to use the LDA-measuring technique (see Section 4.2) for velocity measurements, while in the steel wall holes are made for inserting glass fibre probes (see Section 4.3). 5 rows of 6 holes, with a mutual horizontal distance of 7 cm are placed at heights of 7.5, 17.5, 27.5, 42.5, 57.5 and 77.5 cm, relative to the lower side of the measuring section. The separating plate between the two flows ends at a height of $\pm$ 20 cm in the measuring section. This gives the possibility to investigate the flow before mixing is occurring. The dimensions of the (rectangular) measuring section are 40 cm wide, 20 cm deep, and 150 cm high. These dimensions guarantee that a main part of the flow is not disturbed by boundary effects.

Contraction Just before the measuring section, a contraction is constructed, to give a higher velocity, without increasing the turbulence, but mainly to have the possibility to insert bubbles. A too dense grid of the capillaries of the sparger should result in a direct coalescence of the bubbles. This can be prevented by first generating the bubbles (at a reasonable mutual distance) and increase the gas fraction after it by the contraction section. The section is decreasing from 40 x 60 cm to 20 x 40 cm, so the contraction coefficient is 3.

Honeycomb To decrease the fluctuations in the flow, and to annihilate big eddies possibly created by the bend, two honeycomb structures, each with a length of 10 cm, and a diameter of 5 mm, are mounted inside each of the flow channels. Its structure is shown in Figure 4.3.

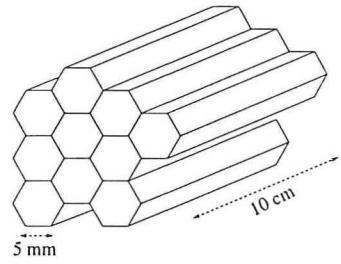

Figure 4.3: Structure of the honeycomb

Knock out vessel After the measuring section, the two phase mixture enters a knock out vessel. This serves to release the air before the water flows into the buffer vessel, to minimise the probability that some air returns with the water flow to the pumps.

4.1.2 Air flow

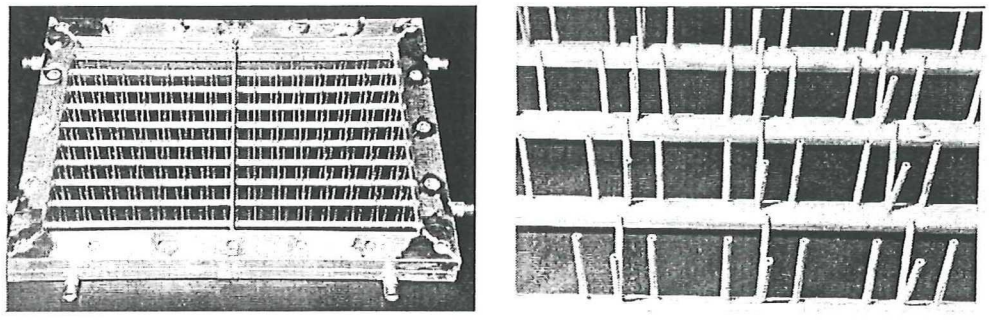

(a) global view (b) detail

Figure 4.4: Photographs of the sparger

To get a good gas distribution, a sparger is constructed. Figure 4.4 shows a photograph of it. It consists of 9 rods at both sides, with an internal diameter of 1 cm, to which

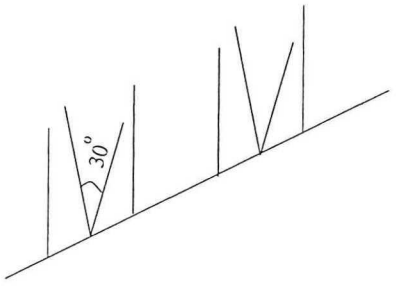

Figure 4.5: Mutual position of the capillaries

the air is led. Upon each rod, small tubes with an internal diameter of 1 mm and a length of 25 mm are placed. Both parts contain ± 250 of these tubes.
The capillaries are placed in groups of 4, with 2 of them vertical, and two under a mutual angle of 30 ° (see Figure 4.5).
The flow meters used are Fischer & Porter precision bore flow rate tubes, types 3f-3/8-20-5/36 and FP-3/0-0-5/36. Their flow ranges are 36 and 64 l/min respectively. The inaccuracy of the air flow meters is estimated as 0.2 lit/min. Details and calibration curves are given in Appendix C.

4.2 LDA-system

For LDA-measuring, the backscatter mode is used. This means that the angle between the incident beam and the scattered signal is 180 °. Other modes are forward- and side scatter (see Figure 4.6).

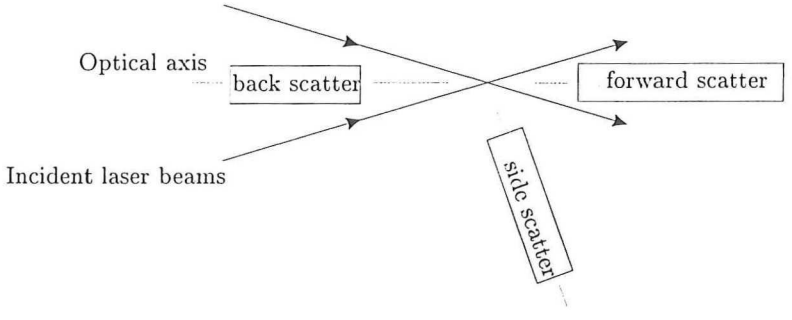

Figure 4.6: Different scatter modes

The total LDA-system consists of several units (see Figure 4.7). The laser is a Spectra-Physics Ar-ion laser (model Stabilite 2016). From the colours, the laser generates, three wavelengths are selected: 514.4 nm (green), 488.0 nm (blue) and 476.0 nm (violet). Using these three colours, the velocities in 3 directions can be measured simultaneously. The total possible supplied power is 4.2 Watt. The colours are separated in a ColorBurst Model 9201 of TSI Inc. A Bragg cell splits the beam, and shifts one of them by 40 MHz. This can electronically be downmixed to a more suitable preshift. The green and blue beams are via two glass fibre probes each brought to a 2D-probe, and the violet beams to a 1D-probe. For the investigations of this project, only the 2D-probe is used. The probes serve for sending and focussing the laser beams, as well as for registrating

the scattered signals. The scattered light is received by a ColorLink, separated by colour, and converted into electrical signals by photo multiplier tubes (PMT). The electronic signals are further processed by the IFA 750 data processor, resulting in the required velocity and time information. Settings of the preshift, the multiplications of

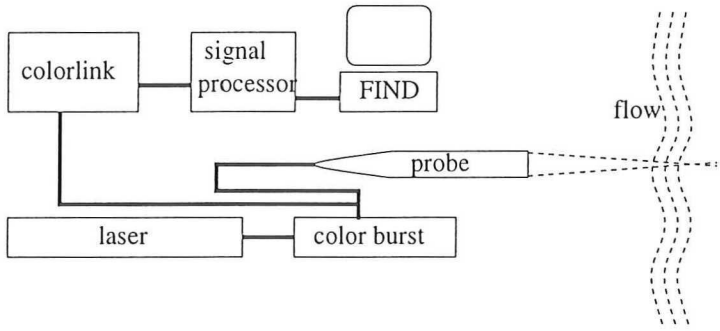

Figure 4.7: Various components of the Laser Doppler Anemometry system

the PMT's etc, can be set by the software, belonging to the LDA system, called FIND (Flow INformation Display).
By means of a lens, the beams are focussed in the measuring volume. Used are lenses with a focal length F of 250, 350 and 500 mm.
The distance between the two beams is 50.0 mm. The diameter of a laser beam D_0 near the lens is 2.10 mm. The dimensions of the measuring volume, calculated with equation 3.8, are displayed in Table A.1 in Appendix A. Also the fringe spacings (equation 3.5) are presented in Appendix A.

Additional LDA - equipment A 486 DX/2 66 MHz Ms-DOS computer was used to run the FIND software. With this software, the IFA 750 parameters can be set. The measured Doppler frequencies and additional burst information (e.g. a time parameter) are stored on the hard disc.
A Tektronix 2225 oscilloscope displayed the Doppler signals continuously. This information was used for setting the noise threshold value, the PMT value and checking burst detection.

Traverse System For measuring at different positions, the LDA-probe is placed at a traverse system, which makes two-dimensional traversing possible.
The inaccuracy in estimated to be 1 mm in the traverse direction, for the positions beneath the end of the splitter plate (here the splitter plate can serve as reference position), and 1 - 2 mm above the separator plate. This inaccuracy is caused by an accumulation of errors in the position determination, the unstiffness of the traverse system, and the inaccuracy in the determination of the relative position of the traverse system to the measuring section.

4.3 Glass fibre probes

The glass fibre probe consists of a metallic capillary (external diameter 2 mm) with a length of 30 cm, containing a glass fibre (see Figure 4.3). The fibre is of the type Fibrosil^{TM}, having a diameter of 0.6 mm. This fibre consists of a kernel of quarts glass, with a diameter of $200 \pm 8 \mu m$, surrounded with a cladding of silicone, to prevent leaving of the light. This is protected with a layer of teflon. The probe can be brought into the

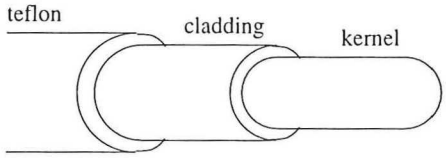

Figure 4.8: Tip of the glass fibre probe

flow through one of the holes in the back side of the measuring section. These holes have

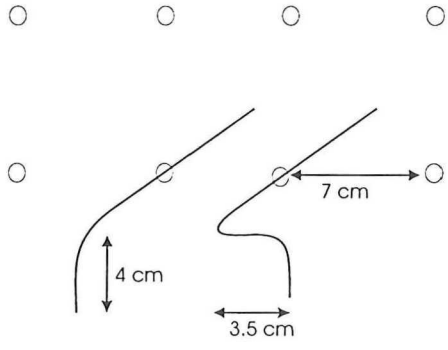

Figure 4.9: Different shapes of the probes

a mutual distance of 7 cm. To get a denser grid, probes are made in different shapes, as depicted in Figure 4.9. This gives the opportunity to measure at more positions, although the mutual distance is still quite big. The end of the fibre is bent over 90° to position the fibre tip vertically. From the end of the fibre the cladding and teflon are removed. At this point the measurement takes place. The point of the fibre is melted to a spherical shape.

At the other end of the fibre, a fibre connector is attached, to connect the fibre to

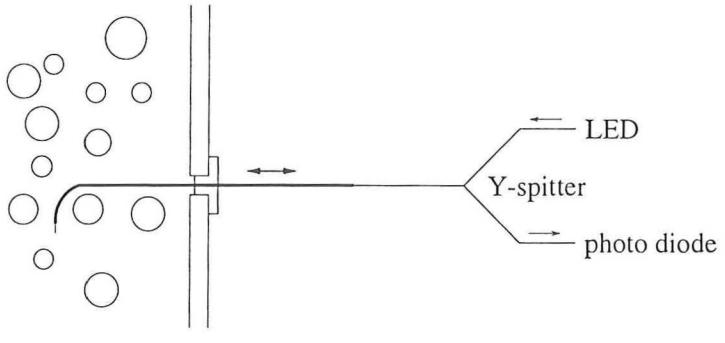

Figure 4.10: Schematic overview of the fibre probe

an acquisition unit, containing a Y-splitter (to split the reflected signal from the one sent), a LED, sending light with a wavelength of 700 nm, and a diode, to convert the light into an electrical signal (see Figure 4.3). This signal is multiplied, and led to a Data Acquisition Unit (DACQ), which calculates the rise and intersection time. An oscilloscope, type Tektronix 2225 is used for checking the shape of the signal. A Ms-DOS computer is used to run the software, used for regulating the measurements. Saved are the rise time and the intersection time of each bubble, plus the total measuring time. From this data, the gas fraction, the mean rise time τ_{rise} and thus an estimate of the velocity can be calculated.

Chapter 5

Results

5.1 LDA settings

For determination of the velocity profiles, the LDA settings, given in Table 5.1 have been used. Measuring dimensions, belonging to the different lenses, as well the fringe spacings, are given in Table A. A measuring time of 100 s is expected to be long enough

Table 5.1: Specifications of the laser Doppler anemometer.

	Channel	
	Green	*Blue*
Wavelength [nm]	514.5	488
Beam spacing [mm]	50	50
Focal length [mm]	250,350,500	250,350,500
PMT setting [V]	900-1200	900 - 1400
	Processor	
	1	*2*
Number of data points [-]	± 17 K	± 3 K
Mean data rate [Hz]	150-250	30-50
Measuring time [s]	60-100	60-100
Acquisition mode	random	random
Single measurement/burst	on	on
Minimal threshold [mV]	20-100	10-50
Filter range [kHz]	30-300	30-300
Preshift [kHz]	0	100
Bias correction	none	none

for getting accurate calculations for the mean and variance (for details, see Appendix E).
The velocities were calculated at the positions, given in Table 5.2.

Table 5.2: Measuring positions (cm) for velocity profiles

y (cm)	+/- 0.25 +/- 3.00 +/- 10.0	+/- 0.50 +/- 3.50 +/- 12.0	+/- 1.00 +/- 4.00 +/- 14.0	+/- 1.50 +/- 5.00 +/- 16.0	+/- 2.00 +/- 6.00 +/- 17.0	+/- 2.50 +/- 8.00
z (cm)	2.0 14.0	4.0 16.0	6.0 18.0	8.0	10.0	12.0

5.2 Mean water velocities

Two flow situations have been investigated: equal velocities on both sides, with a mean velocity $U_1 = U_2 = 0.6$ m/s (called situation 1) and a difference in velocity: $U_1 = 0.82 \pm 0.01$ m/s, and $U_2 = 0.54 \pm 0.01$ m/s, so $\Delta U = 0.28$ m/s, called situation 2. Both situations are discussed below.

5.2.1 Initial flow

To investigate the assumptions, used for describing the mixing layer, the splitter plate (which first ended before the measuring section) has been made higher. This offers the possibility to measure velocities before mixing is occurring.

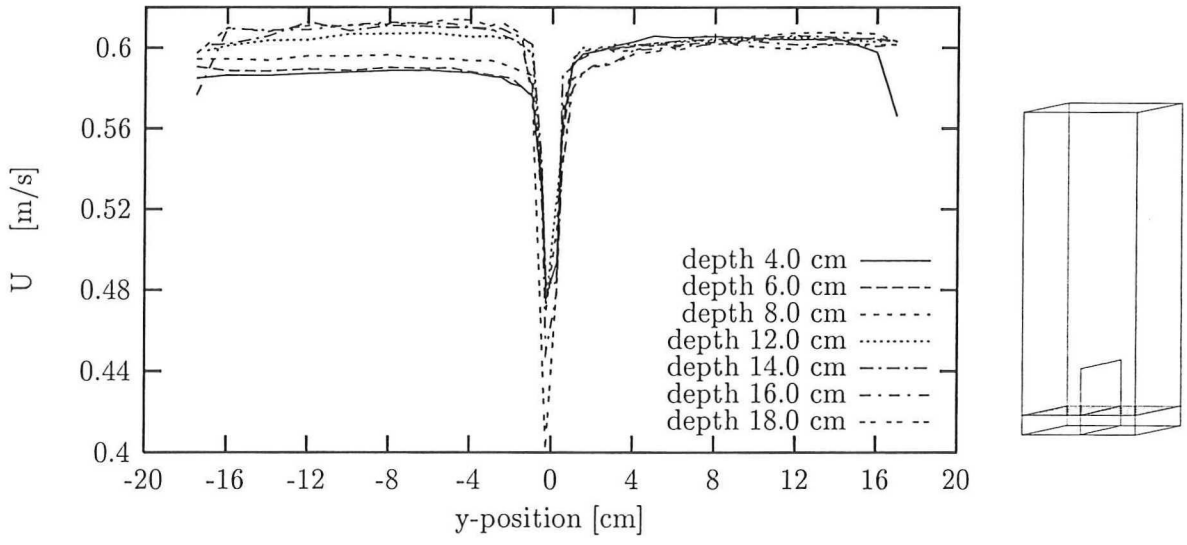

Figure 5.1: Initial mean velocity profiles, for equal velocities (situation 1).

The profiles of situation 1 are depicted in Figure 5.1. The flows are, according to the flow meters: $U_1 = 0.590 \pm 0.008$ m/s and $U_2 = 0.610 \pm 0.008$ m/s.

The following results can be seen from Figure 5.1:

- A boundary layer exists at both sides of the splitter plate. This layer has at this

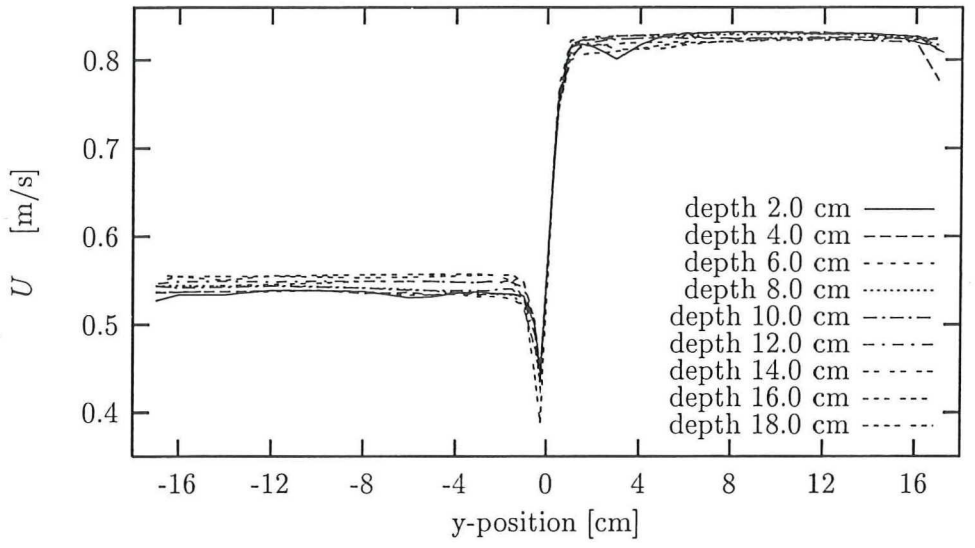

Figure 5.2: Initial mean velocity profiles, for different velocities (case 2).

height, a thickness of about 1 cm. This agrees with the theoretical value for this situation, according to equation 2.36, when assuming an x-position of $\approx$ 50 cm.

- The profiles on the left side are not exactly equal for different depths (The value for the depth represents the distance from the front wall). An increase of $\approx$ 3 cm/s with depth is seen. It probably is caused by the widening of the tube before the bend.
  The influence of the gradient in z-direction on the development of the mixing layer is expected to be negligible. It maintains naimly almost constant for different heights.

- A small difference exists between the expected and the measured velocities. Probably it's caused by the obliquity of the splitter plate of several millimetres to the right. This results in a increase of the mean flow at the right side, and a decrease at the left, of 1 à 2 %.

- The profiles have been measured till 17 cm from the separator to both sides, and not to the walls of the section. Flanges at the edges of the measuring section make it impossible to determine the velocities over the last centimetres.

Also situation 2 is observed, giving the results shown in Figure 5.2. The same remarks, made for Figure 5.1, can be made here. But an important fact is the disagreement between the calculated velocities according to Appendix B, and the measured quantities. From the flow meters follows: $U_1 = 0.853 \pm 0.006$ m/s and $U_2 = 0.500 \pm 0.006$ m/s , while these values clearly differ from the measured ones. This suggests that somewhere between the water-flow meters and the measuring section, a leakage exists between the two parts. To check this, several experiments have been done. The first one, is reversing the velocity difference, with $U_1 \approx 0.50$ m/s, and $U_2 \approx 0.84$ m/s (so U_1 is now lower

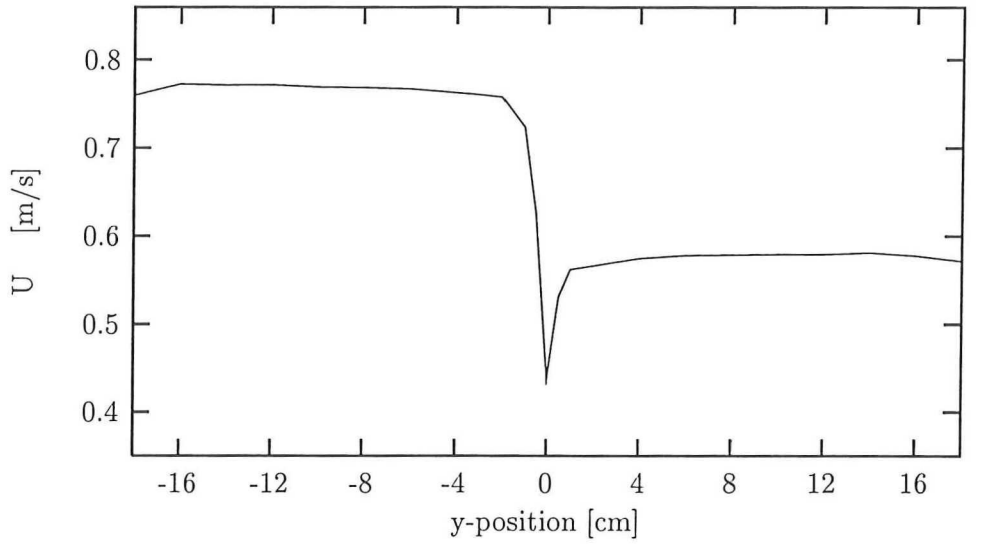

Figure 5.3: Mean velocity profile with the left velocity high, the right one low (depth = 10 cm, height 3 cm).

than U_2). The result is shown in Figure 5.3. As expected, also here, the low velocity increases with respect to the flow meter, and the higher one decreases.

Leakage estimation To estimate the amount of leakage between the two parts, the velocities shown in Figure 5.2 are integrated over the whole surface. The following equation is used:

$$\Phi = \sum_{i=2,j=2}^{i=16,j=8} U_{i,j} * \frac{|y_{i+1} - y_{i-1}|}{2} \frac{|z_{j+1} - z_{j-1}|}{2} \tag{5.1}$$

in which $U_{i,j}$ is the measured mean velocity at position (y_j, z_i) (expressed in cm), where y_i and z_j take all the values given in Table 5.2, except the first and last values. For them, Equation 5.1 cannot be used, because of the missing of $_{-1}$ or $_{+1}$ values.
When, for instance, i = 1, the following approximation is used:

$$\Phi_{i=1} = \sum_j U_{1,j} * |y_2 - y_1| \frac{|z_{j+1} - z_{j-1}|}{2} \tag{5.2}$$

The other boundary positions are done in an equivalent way. In this way the flow from $(y, z) = (0.125, 1.0)$ till $(17.5, 19.0)$ can be calculated. The flow in the part from $y = 0$ to $y = 0.125$ cm is negligible; the flow from $z = 0$ to $z = 1.0$ and from $z = 19.0$ to $z = 20.0$ is approximated by assuming the same velocity profile as from $y = 0$ to $y = 1$ cm. The same is done for $y = 17.5$ to $y = 20.0$ cm.
The results of this calculation are given in Table 5.3. Although the values for the difference don't agree, from this table can be concluded that a flow exists from the high-velocity flow to the low one. The calculation of the inaccuracies is given in Appendix E. Possibly, the problem is caused by the small gaps in the splitter plate. They are caused by the different units, the setup consists of. The different parts of the splitter plate do not join exactly, causing the gaps.

Table 5.3: Comparison of calculated with measured flow

	LDA (lit/min)	flow meter (lit/min)	difference (lit/min)	deviation (cm/s)
flow left	1278 ± 30	1195 ± 20	+ 83 ± 36	+ 3.4
flow right	1927 ± 30	2047 ± 15	-120 ± 33	- 5.0

Horizontal velocity Besides the main flow, also the horizontal velocity is measured. This is done to investigate the isotropy of the turbulence.

Because of the not exactly horizontal plane of the laser beams, a component of the

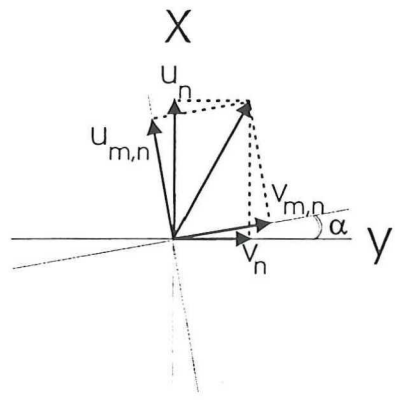

Figure 5.4: The measured and the real velocity vectors

vertical velocity is measured. This can be seen from Figure 5.4, showing:

$$u_{m,n} = u_n \sin\alpha - v_n \cos\alpha \tag{5.3}$$

$$v_{m,n} = v_n \cos\alpha + u_n \sin\alpha \tag{5.4}$$

where $u_{m,n}$ is the instantaneous measured velocity component in (almost) vertical direction, $v_{m,n}$ that in horizontal direction, and u_n and v_n the real vertical and horizontal velocity components. α is the angle between $u_{m,n}$ and u_n. Using $u_n = U + u'$ and $v_n = v'$ (the mean component of v_n is assumed to be zero) the following relations can be derived:

$$\overline{v_{m,n}} = \frac{1}{N}\sum_{n=1}^{N} v_{m,n} = U \sin\ \alpha \tag{5.5}$$

$$\overline{v'^2_{m,n}} = \overline{v'^2_n}\cos^2\alpha + 2\sin\alpha\ \overline{u'_n u'_n} + \overline{u'^2_n}\sin^2\alpha \approx \overline{v'^2_n} \tag{5.6}$$

$$\overline{u'^2_{m,n}} \approx \overline{u'^2_n} \tag{5.7}$$

$$\overline{u'_{m,n}v'_{m,n}} = \overline{u'_n v'_n}\ \cos 2\alpha + \cos\alpha \sin\alpha(\overline{u'^2_n} - \overline{v'^2_n}) \tag{5.8}$$

The last term gives some problems, because $\overline{u'_n v'_n} << \overline{v'^2_n}$. The term $\overline{u'_n v'_n}\cos^2\alpha$ is estimated to be of the same order as $\overline{v'^2_n}\cos\alpha\sin\alpha$. This holds if α is small. Only assuming $\overline{v'^2_n} \approx \overline{u'^2_n}$, the last term in equation 5.8 is zero, and the measured stress $\overline{u'_m v'_m}$

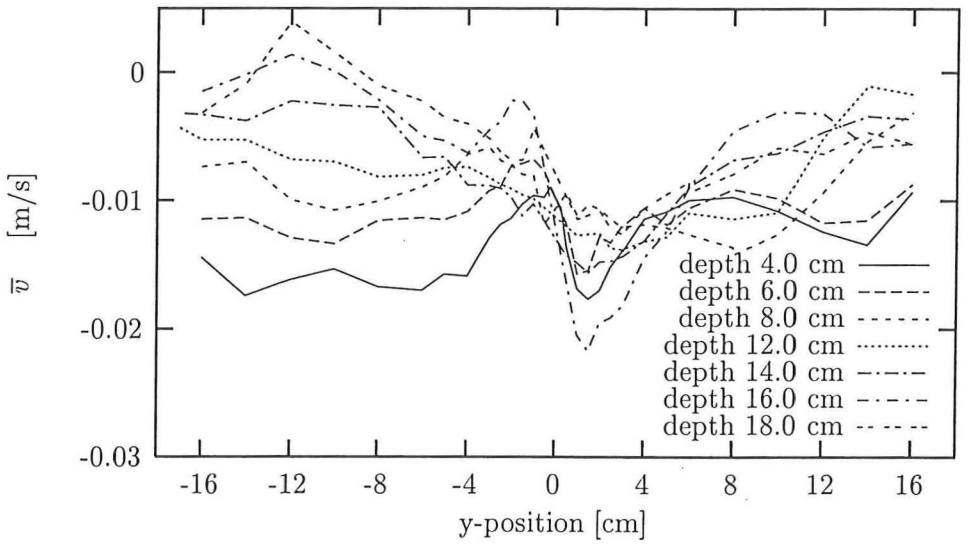

Figure 5.5: Horizontal initial velocity profiles, for equal velocities.

approximates the real stress.

As mentioned above, the measured mean horizontal velocity can be correlated with the angle α, using equation 5.5. However, Figure 5.5 shows that no unique horizontal component is derived. This can be caused by the small set of data points ($\approx$ 3k) for averaging, resulting in a large uncertainty of the calculated average. Another possibility is the change of the angle α while traversing. The increase of the measured horizontal velocity with depth can be ascribed to the increase of the vertical component with depth. A global value for $\overline{v_{m,n}}$ of -1 cm/s corresponds to an angle α of ≈ 1 °.

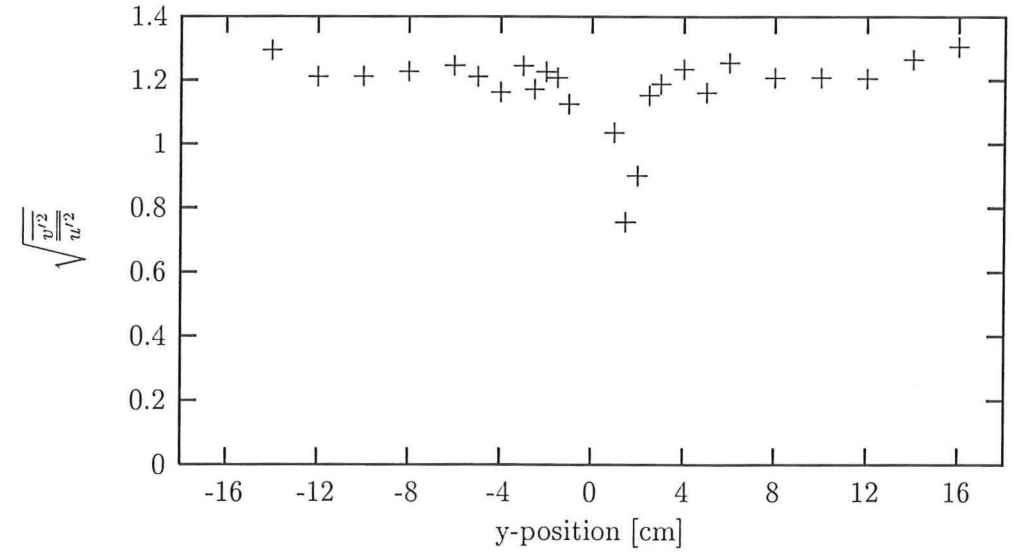

Figure 5.6: The ratio of fluctuating terms (case 1, depth 12 cm).

Horizontal fluctuating velocity For isotropic flow, the standard deviations (equation 2.18) are the same for all directions. In Figure 5.6, the ratio between the vertical and the horizontal component is depicted. It shows that the horizontal component follows the vertical one (which is forced by the flow conditions), and that the horizontal one is bigger than the vertical one by a factor 1.2. This value is clearly higher than the value of Lance, who gives $\sqrt{\frac{v'^2}{u'^2}} = 1.02$. So no isotropic flow occurs in the initial flow. When reminding that most turbulence is induced by the bars of the sparger, the flow can be seen as turbulence induced by a grid of bars. Bradshaw [1971] mentions a ratio of 1.15 for this situation. This is in good agreement with the measured values.
Figure 5.7 shows the ratio of the Reynolds stress $\overline{u'v'}$ to the normal stresses $\sqrt{\overline{u'^2}}\sqrt{\overline{v'^2}}$.

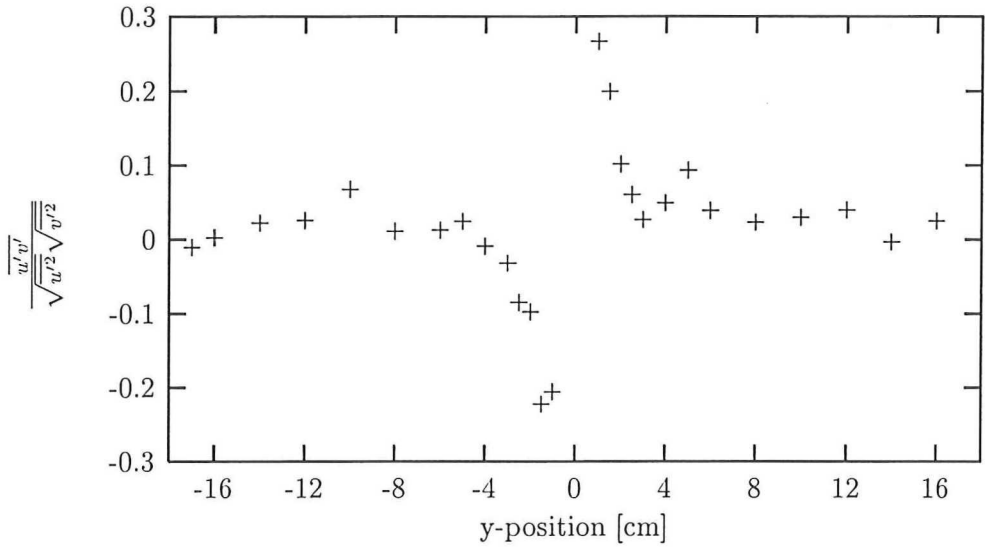

Figure 5.7: The relative Reynolds stress (depth 12 cm; 2.5k data points per position).

Lance [1991] gives $\frac{\overline{u'v'}}{\sqrt{\overline{u'^2}}\sqrt{\overline{v'^2}}} = 0.04$, outside the mixing zone. This value doesn't contradict with the results given in Figure 5.7, because also in the values of Lance, a spreading from -0.8 to 0.8 is found.
Velocities in the z-direction have been done, but the data rate was too low to determine the standard deviation with any sense.

5.2.2 Development with height

Besides investigating the initial flow conditions, the velocities have also been measured as a function of height. Here, not the total cross section is investigated, but only the profile halfway between the glass and the steel wall. Figure 5.8 shows the results for the equal-velocity case (situation 1), and Figure 5.9 for case 2. The profiles are not exactly horizontal outside the mixing zone. The reason is unknown.

Assumed in theoretical mixing layers is that the level of the undisturbed velocity maintains constant. Remarkable is the disagreement of the profiles in Figure 5.9 at the left side, while the profiles agree well at the right side. This effect could be caused by

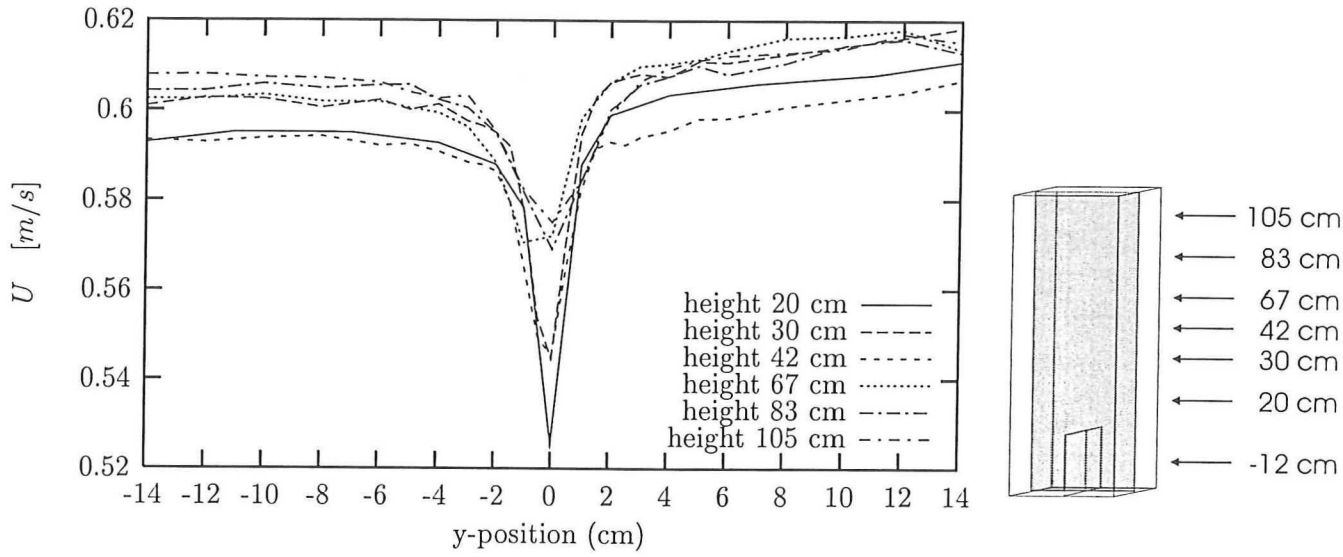

Figure 5.8: Mean velocity profiles for different heights (depth 10 cm).

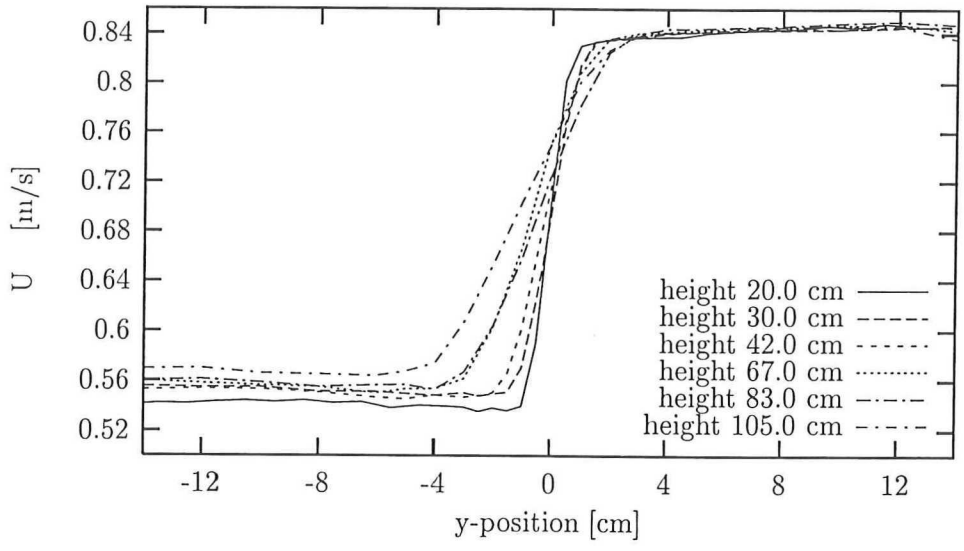

Figure 5.9: Mean velocity profiles for different heights (depth 10 cm).

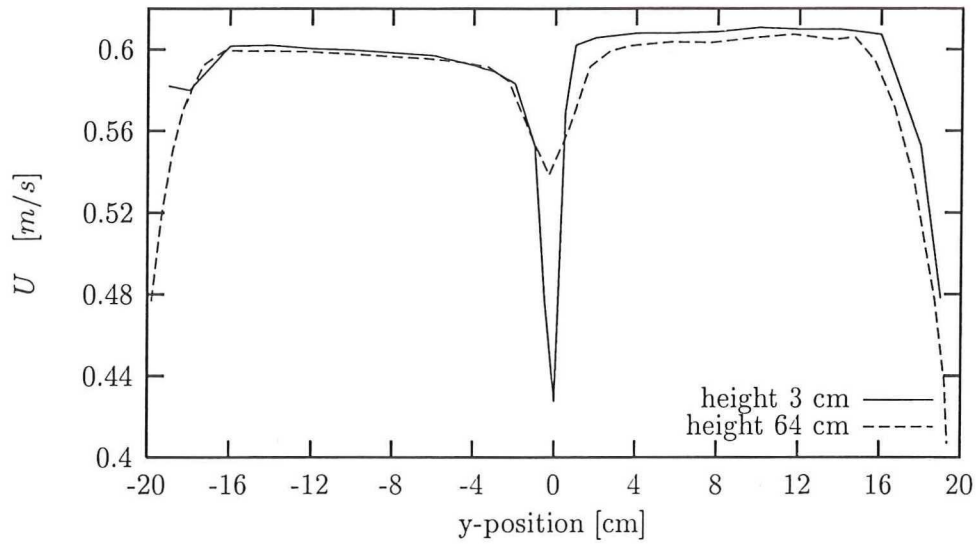

Figure 5.10: Mean velocities at different heights without changes of the flow rate.

the fact that these measurements were done with not exactly equal adjustments of the water flow, because they were done in different runs. An accurate adjustment of the flows is possibly influenced by the leakage. Measuring the velocity profiles at different heights without changes at the supply, give a small decrease of the level, falling inside the inaccuracy of the measured flows (Figure 5.10).

Development of $y_{1/2}$ From Figure 5.9 follows that the point $y_{1/2}$ (defined as the y-position where the velocity equals the mean of U_1 and U_2, see also 2.3) is moving to the left. The change of this point with height, is shown in Figure 5.11. As mentioned in Section 2.3, a linear relation between $y_{1/2}$ and x is expected, which agrees moderate with the experimental values. Fitting a straight line through the experimental values for $y_{1/2}$ gives:

$$y_{1/2} = (0.0114 \pm 0.0002)x - (0.24 \pm 0.11) \tag{5.9}$$

with $y_{1/2}$ and x in cm. Roig [Roig, 1993] gives (for this situation): $y_{1/2} = (0.004 - 0.009)x$ so these values contradict. The deviations are probably caused by the inaccuracy of the zero-point determination, as the position of the splitter plate could not be measured in the situation before it was made higher.

Development of B(x) Another important aspect of mixing layers is the development of the width B of the mixing zone. According to Roig [1993] the width of the layer is defined as the distance between the points where the flow increases from $U_2 + 0.1\Delta U$ to $U_1 - 0.05\Delta U$:

$$B(x) = |y(U = U_{low} + 0.1\Delta U) - y(U = U_{high} - 0.05\Delta U)| \tag{5.10}$$

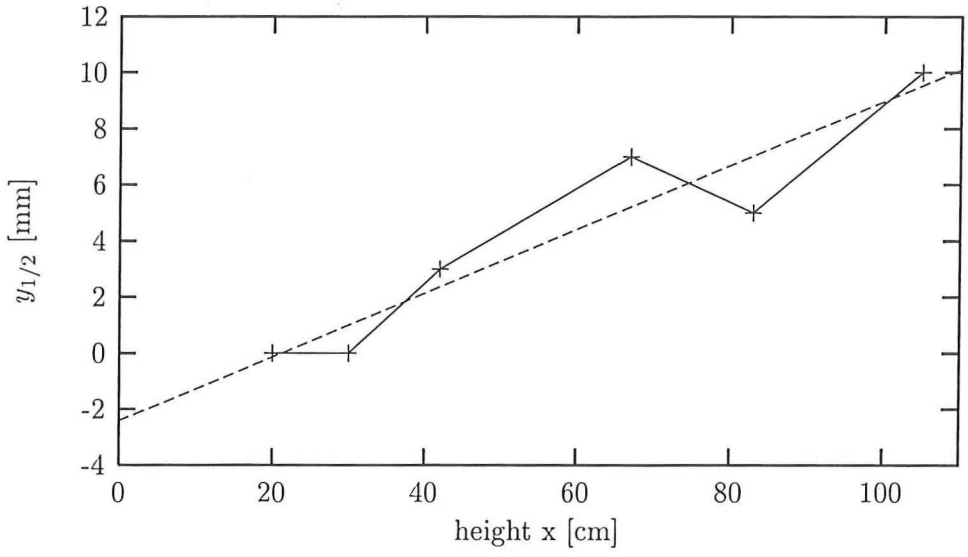

Figure 5.11: Position of the $y_{1/2}$ point for different heights.

The development of the width with height, is shown in Figure 5.12. As expected from Equation 2.3, the width of the mixing zone B grows linearly with height. The following line is fitted:

$$B(x) = (0.456 \pm 0.099)x + (0.61 \pm 0.07) \tag{5.11}$$

Both $B(x)$ and x are expressed in cm. Brown and Roshko [1974] found an offset of -6.2 mm for x, when $\lambda = 0.75$, while here an offset of -13 cm is found. This difference is probably caused by the differences in the setup. No offset is reported by Roig [1993]. When considering the influence of the thickness of the used splitter plate (2mm) and of the boundary layer of the plate, a starting layer width of 6 mm is acceptable.

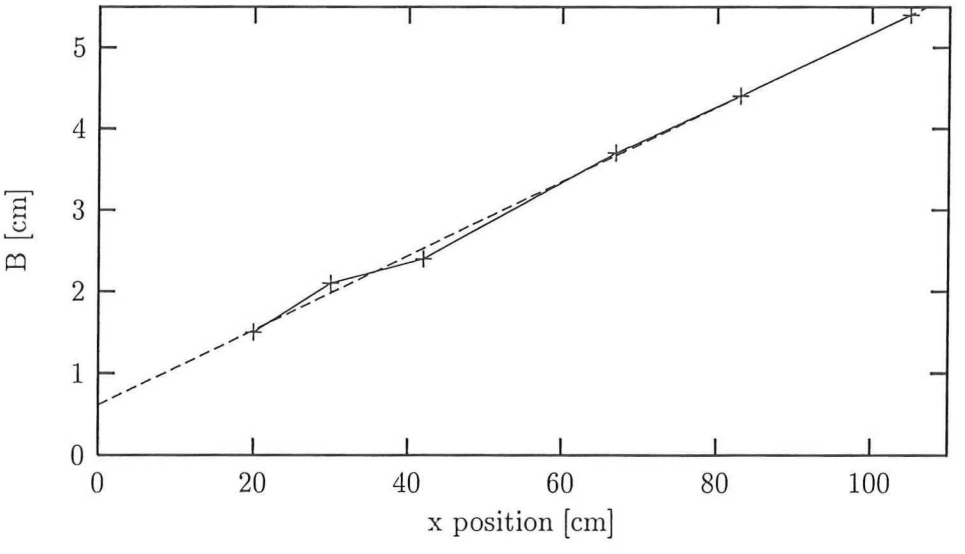

Figure 5.12: Width of the mixing zone for different heights.

5.3 Fluctuating velocities

5.3.1 Initial flow

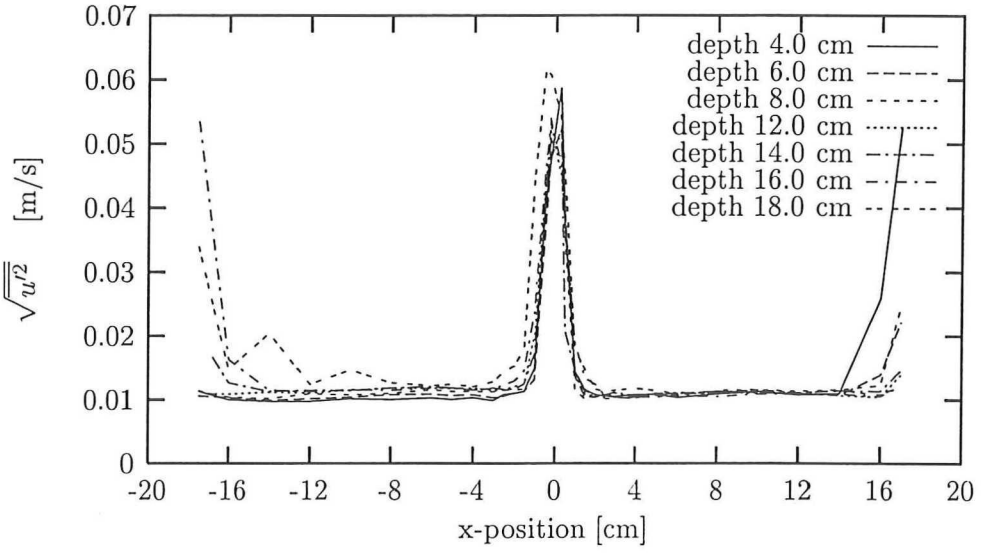

Figure 5.13: Initial standard deviation profiles, for case 1

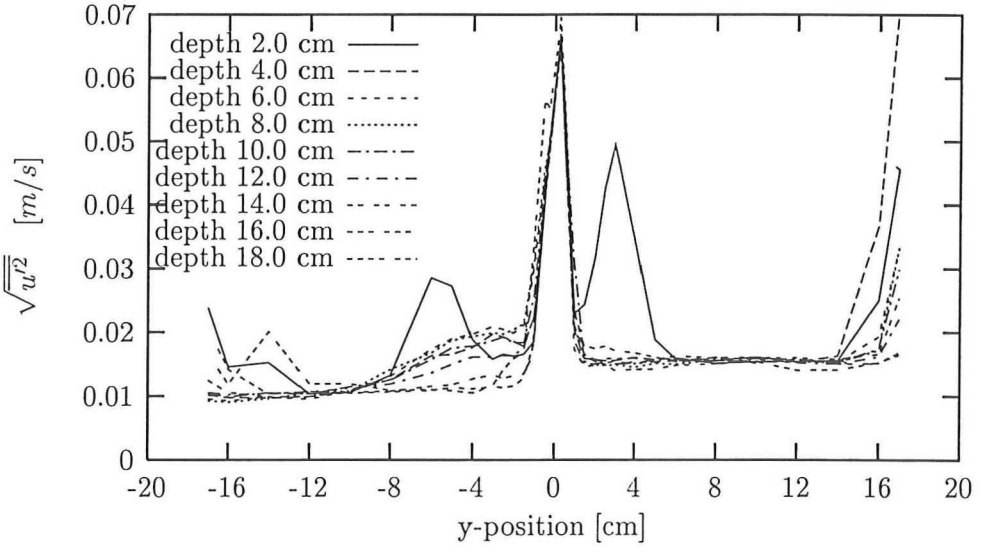

Figure 5.14: Initial standard deviation profiles, for case 2.

Besides the mean flow, also the fluctuations around the the mean flow, defined by Equation 2.47, is calculated. As mentioned in Section 2.4, the standard deviation $\sqrt{\overline{v_i'^2}}$ is a measure for the intensity of the turbulence of the flow. Figure 5.13 shows the initial fluctuating-velocity profiles, for case 1 (i.e. the standard deviation in velocities for the profiles of Figure 5.1). The following facts can be derived from Figure 5.13:

- Besides some influences of the wall, the profiles are flat.
- The vertical turbulence intensity I_x in the undisturbed region amounts 2 % for both sides. The same value is given by Lance [Lance and Bataille, 1991].
- The splitter plate induced turbulence results in a sharp peak.

The fluctuations for case 2 (related to Figure 5.2) are depicted in Figure 5.14. Besides the remarks made at Figure 5.13, can be seen from this figure:

- The peaks in the profile at a depth of 2 cm are caused by unevenesses at the wall. They correspond with the small dips in the mean velocity profile in Figure 5.2. The same holds for the 18 cm-profile. The strong increase at the right could be caused by the influence of the wall, but this effect is much smaller at the left wall. Comparison with Figure 5.2 shows that in the right front-edge, and in the left back-edge, an extra amount of turbulence in induced by ruggednesses in the setup.
- The absolute turbulence of the right side is higher than at the left side, but the (relative) turbulence degrees are both low, i.e. < 2 %.
- A slight increase of turbulence exists just left of the separator-peak (from -2 to -8 cm). The reason is unknown. It is not seen in Figure 5.13.

5.3.2 Development with height

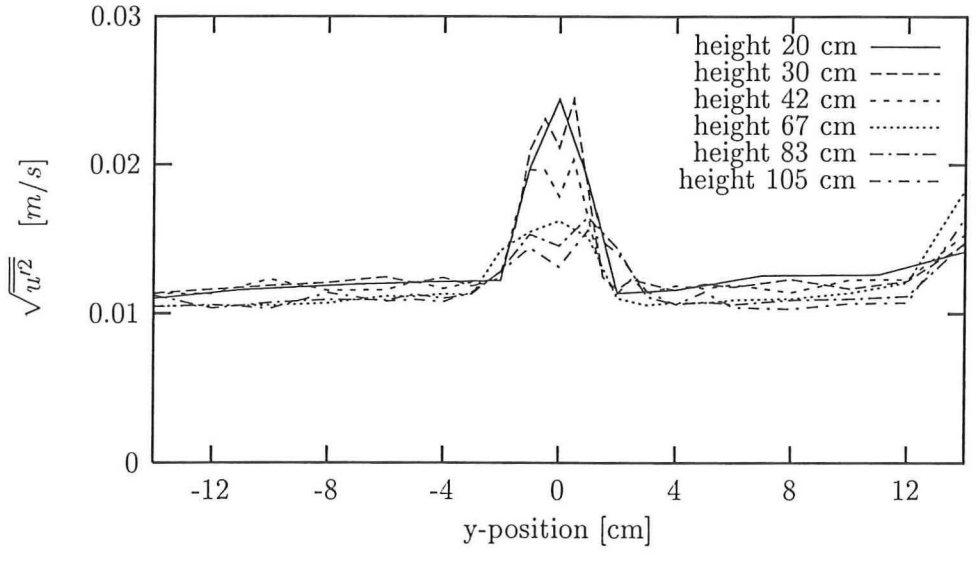

Figure 5.15: Standard deviation profiles, for case 1 for different heights (depth 10 cm).

The fluctuations for the equal-velocity-case, belonging to Figure 5.8, are depicted in Figure 5.15. As expected, the peak becomes both lower and wider with increasing

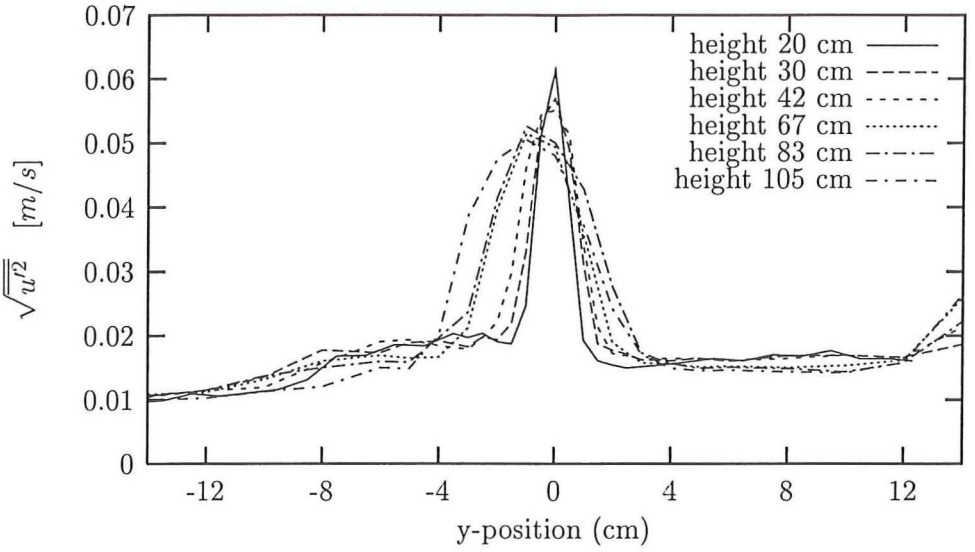

Figure 5.16: Standard deviation profiles for case 2 for different heights (depth 10 cm).

height. Outside the mixing region, a slight decrease of turbulence intensity seems to exist. This can be compared with the equation, Lance [1991] gives for it:

$$\frac{u'}{U} \sim x^{-1.16} \tag{5.12}$$

A more accurate investigation shows that the values for the standard deviation are constant, within the accuracy of the measurements. Another aspect is that equation 5.12 is valid after $\approx$ 1 m.

The fluctuations for the different-velocity-case, related to Figure 5.9, are depicted in Figure 5.16. The same remarks, made at Figure 5.15, can be made here. What also can be seen, is the movement of the position of the peak. This agrees with Figure 5.11, where the $y_{1/2}$-position is depicted. The decrease of the intensity with height is not detected in this figure.

Notice the different scales, used for the equal- and the different-velocity cases.

5.4 Dimensionless profiles

As mentioned in Section 2.3, the mean flow can be described in a dimensionless form. Scaling with the local velocities, using a value of 36 for χ, gives the profiles of Figure 5.17. For χ, not the estimate according to Sabin (eq. 2.7) is chosen, but that of Miles [Roig, 1993, page 96]. He proposes:

$$\chi \approx \chi_0 \left(1 + 5(\frac{U_2}{U_1})^2\right) \tag{5.13}$$

where $\chi_0 \approx 11$. This approximation gives the value 36 for the observed case, while Equation 2.7 should give $\chi = 56$. When using 36, an excellent agreement exists between the experimental and theoretical values.

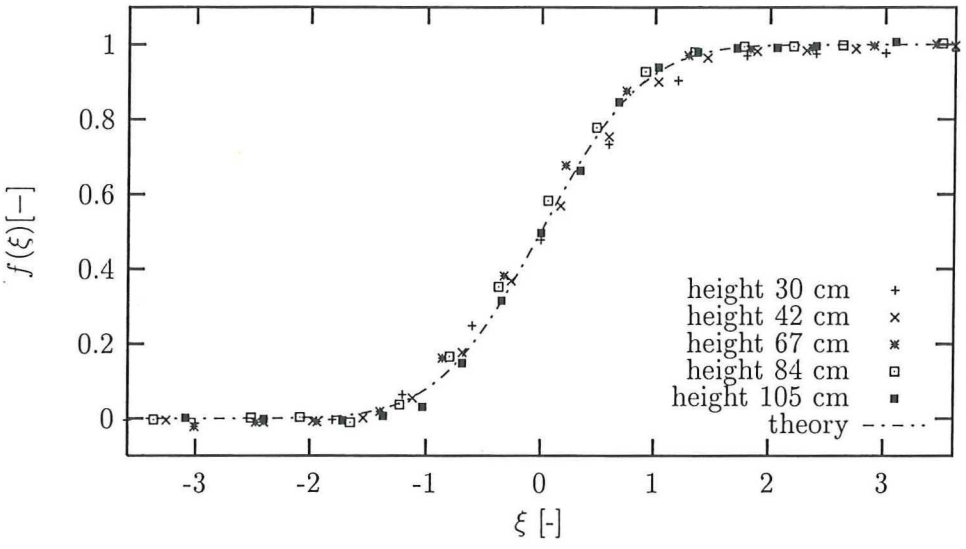

Figure 5.17: Dimensionless profiles for different heights.

5.5 Spectrum Analysis

A requirement of using the Fourier transformation for determining the frequency spectrum, is having an equal time sampled signal. Because the LDA technique gives a Poisson distributed inter particle arrival time (see Section 3.1.3), the data has to be resampled. Used is a linear interpolation between the measurements. As resample frequency, the mean data rate is taken, being the total amount of detections divided by the total time. (As described by Adrian [1987], sampling with a higher frequency is possible, because a probability exists to have smaller inter particle arrival times, following from the Poisson distributed character of the TBD. But the accuracy decreases rapidly for these frequencies.)
Sampling with the mean data rate results in a spectrum up till half the data rate, because of the Nyquist criterium (see Section 2.5).
For a position in the undisturbed flow, outside the mixing layer (x,y,z) = (10,10,-12) (cm), the spectrum is shown in Figure 5.18 for different resample frequencies. For all these spectra, the data is divided into blocks with a duration of 1.64 s. After this time, no correlation is expected any more. Taking a longer time will increase the inaccuracy, because the signal has to be divided into less blocks. To this dataset is referred as case A.
As mentioned in Section 2.5, a slope of $-5/3$ is expected in the inertial subrange. This range goes from $f = U/L$ till $f_K = 1/\tau_K$. Using $U = 0.6$ m/s, and $L = 0.20$ m (i.e. the dimensions of one part of the section) the range is expected to start at $f \approx 3$ Hz. For estimating the high range, the Kolmogorov time scale has to be calculated. Using equations 2.28 and 2.24, with the friction factor f = 0.01, $U = 0.6$ m/s, and $D_h = 0.2$ m, a value of 147 Hz is found for f_K.
Although the data rate of 156 is too low to derive the spectrum till this frequency, the slope of $-5/3$ is expected to be found. From Figure 5.18 follows that a slope of

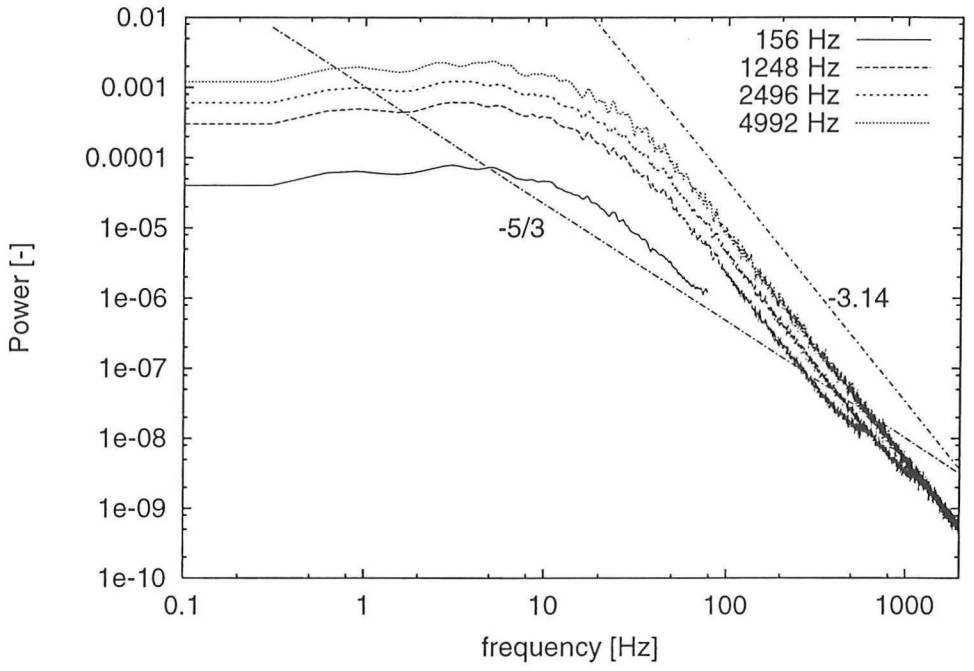

Figure 5.18: Spectra outside the mixing zone for case A, resampling with different frequencies (mean data rate 156)

$\approx$ -2 is found for resampling with the mean data rate, up till -3.14 for high resample frequencies. After f $\approx$ 1000 Hz, the slope maintains constant.

To find out, what the reason is for the disagreement in the slope, also the autocorrelation function (defined by equation 2.43) is investigated. It is depicted in Figure 5.19. A slight disagreement is seen between the different functions. This is caused by the differences in accuracy for the functions, because not all functions are divided in the same amount of blocks (see Appendix D for details). Calculating the integral time scale $\mathcal{T}$ (defined by equation 2.39) by integrating the function of Figure 5.19, is not very reliable. This is caused by the quite low accuracy, because of the relative small number of blocks (varying from 74 to 389), and of the present noise in the 'tail' of the correlation function. After τ = 0.4 s, the autocorrelation is assumed to be zero; all deviation from zero after this time can be attributed to noise. To take this in account, the sum over the autocorrelation function up to this value is also calculated.

Another measure for the integral time scale can be defined as $\int_0^\infty |\rho(\tau)|\ d\tau$. Its (discretized) value is also given in Table 5.4. This table shows that the calculation of the integral time scale is quite dependent on the resample frequency, and the range over which is integrated.

The most reliable value is probably that for 156 Hz, integrated till T = 0.4 s, because for this calculation the largest number of blocks could be taken, resulting in a smallest contribution of the noise. Calculating $\mathcal{T}$ up to T = 0.25 s for this situation gives a value of 13.2 10^{-3} s (vs 12.8 10^{-3}) s.

A theoretical value, according to equation 2.40, gives 0.11 s, when using L = 0.2 m. Taking into account that the situation can be seen as a grid of bar-induced turbulence,

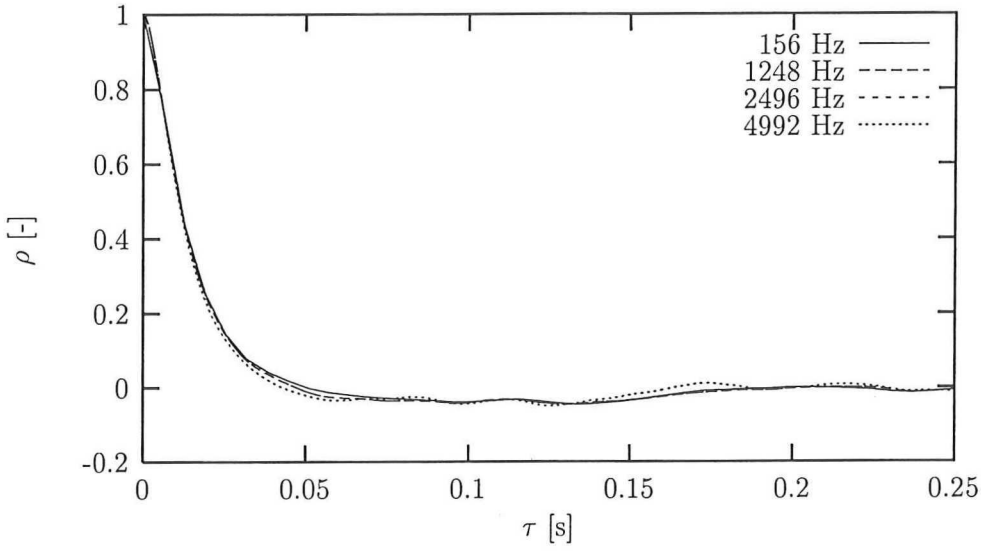

Figure 5.19: Autocorrelation function outside the mixing zone for case A, for different resample frequencies (mean data rate = 156)

Table 5.4: Different values for $\mathcal{T}$ (s), for case A

	156 Hz	**1248 Hz**	**2496 Hz**	**4992 Hz**
$\sum_0^N \rho(\tau)\ d\tau$	$8.60\ 10^{-3}$	$5.41\ 10^{-3}$	$5.21\ 10^{-3}$	$5.83\ 10^{-3}$
$\sum_0^N \lvert\rho(\tau)\rvert\ d\tau$	$26.6\ 10^{-3}$	$24.0\ 10^{-3}$	$23.8\ 10^{-3}$	$22.2\ 10^{-3}$
$\sum_0^{T=0.4} \rho(\tau)\ d\tau$	$12.8\ 10^{-3}$	$9.49\ 10^{-3}$	$9.29\ 10^{-3}$	$8.79\ 10^{-3}$

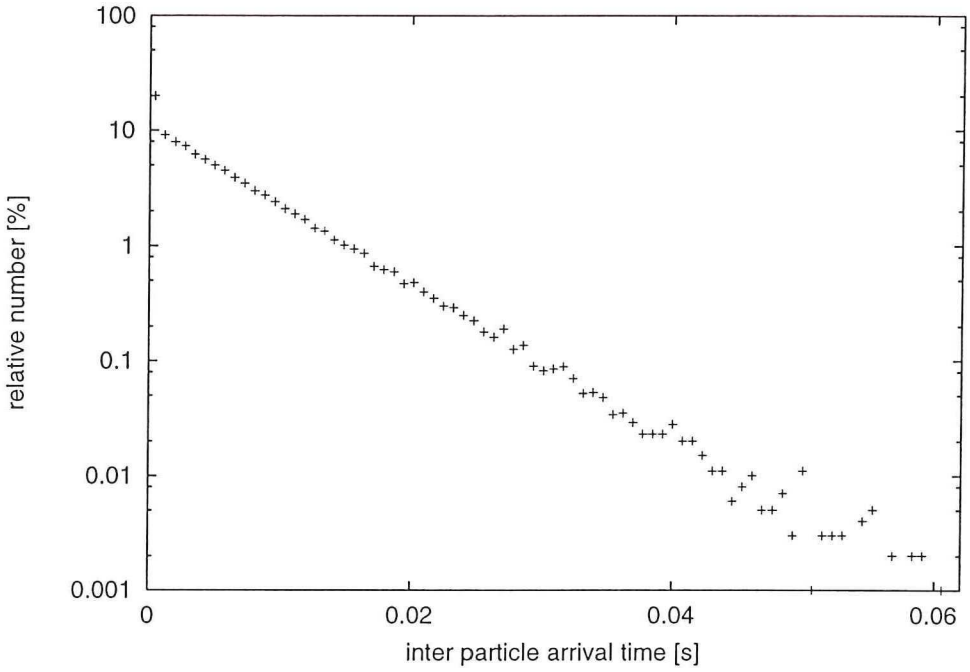

Figure 5.20: Inter particle arrival time for case A

also the distance between the bars (= 4 cm) can be taken as reference length. This results in a value for $\mathcal{T}$ of 22 10^{-3} s. This is in reasonable agreement with the measured values.

The inter particle arrival time for case A is depicted in Figure 5.20. The expected linear relation (on a logarithmic vertical scale, see Section 3.1.3) is found, although the first bin is much higher than expected.

A possible reason for the deviating results for both the spectra and the integral time scales, when using different resample frequencies, could be that the data rate is too low for reconstructing all fluctuations of the flow. Figure 5.21 shows a part of the velocity signal, with linear interpolation. Although it seems to give a reasonable representation of the real flow, also an other situation, with a mean data rate of 827 (vs. 156 for case A) is investigated. To this situation is referred as case B. It is measured at the position (x,y,z) = (10,10,69) (cm).

The higher data rate offers the possibility to follow higher fluctuations in the flow. The effect of the interpolation is expected to decrease.

Figure 5.22 shows the spectra for case B, for different resample frequencies (details about the calculations are given in Appendix D). In Figure 5.22, the slopes go from -0.71 for 250 Hz, to -2.52 for 8000 Hz. A final slope of -3.14 (as in case A) is not seen here. This means that, even for the highest resample frequencies, new information is found in the signal. This becomes clear from the inter particle arrival time distribution, shown in Figure 5.23. It shows a strong pile up of detections for (very) low inter particle arrival times. It can be seen that ± 70 % of the arrival times is less than 0.001 s. Of course, it has a tremendous influence upon the spectrum, when the velocities, measured by successive detections, are different. This will increase the contribution of

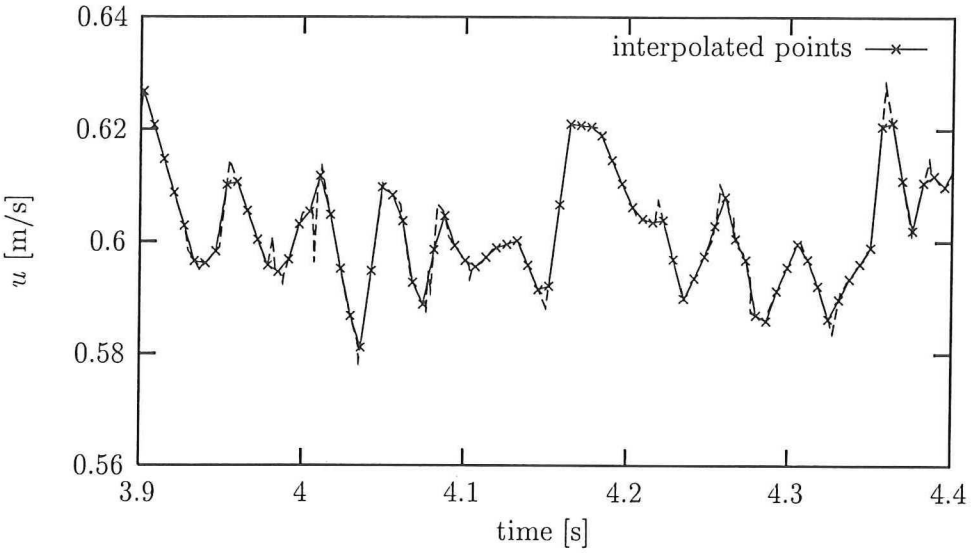

Figure 5.21: Characteristic velocity signal for case A.

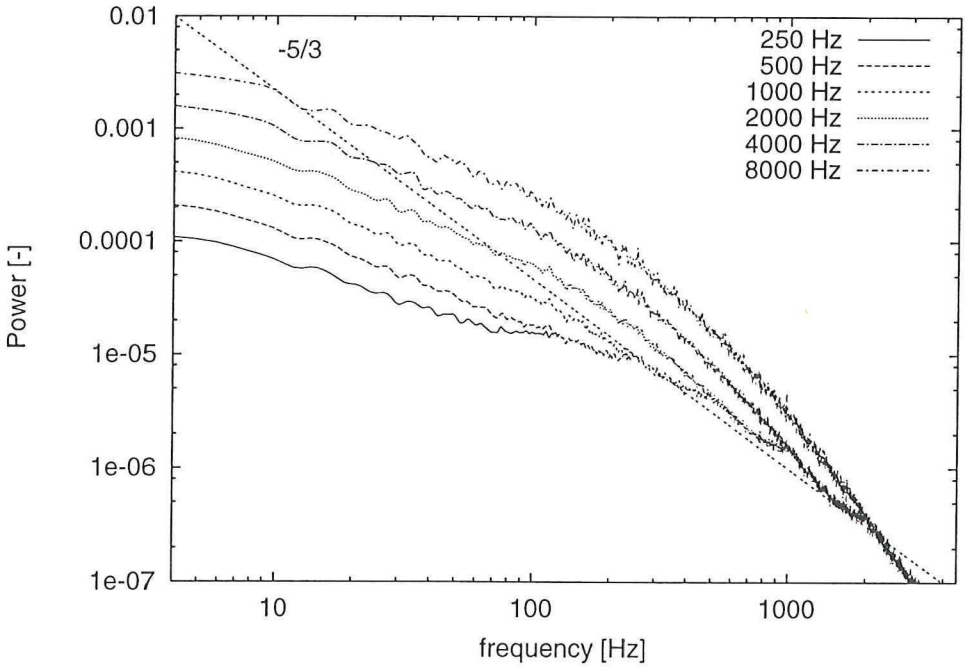

Figure 5.22: Spectra for case B, for different resample frequencies, (Mean data rate = 827)

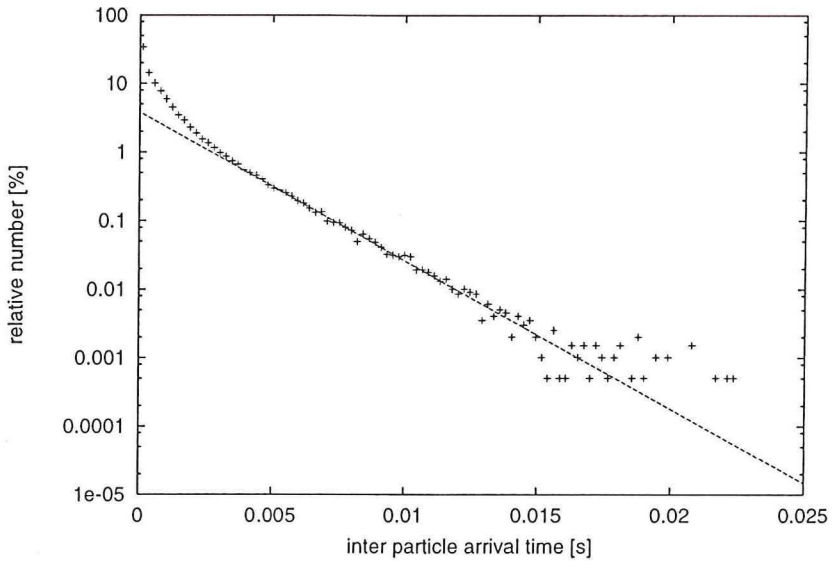

Figure 5.23: Inter particle arrival time, indicating multiple validation (case B)

the higher frequencies, resulting in a smaller slope (i.e. less negative) than in a same situation with a Poisson distributed inter arrival time.

The deviation from the Poisson distribution of the inter particle arrival times is possibly caused by multiple validation [Maanen, 1996]. This means that one particle, moving through the measuring volume, is detected more than once. With the LDA software is adjusted that only one measurement per burst is done. However, assumed is that a burst, while passing the measuring section, has a short dip in scattered intensity. When it lights up again, it is detected as a new particle, resulting in multiple validation.

Multiple validation can be checked by comparing the smallest inter particle arrival times with the duration that a particle moves through the measuring volume. Taking a velocity of 0.6 m/s, the length of the measuring volume being $\approx$ 0.1 mm (see Appendix D), and the smallest inter particle arrival time 3 10^{-5} s, shows that indeed multiple validation can occur, where the particle has only moved a distance of 0.018 mm, when a new detection takes place. So all inter particle times smaller than 1.66 10^{-4} s can be described to multiple validation. However, the deviation from the Poisson distribution is not limited to this time, but goes on till $\approx$ 5 10^{-3} s. No explanation is known for this fact.

The velocity signal for case B is given in 5.24. It shows that indeed very high fluctuations exist in the signal.

The autocorrelation function for case B is given in Figure 5.25. The integral time scale $\mathcal{T}$ for these functions is given in Table 5.5. Comparison of Table 5.5 with 5.4 shows that the integral time scales for case B are smaller than for case A. For Table 5.5 a duration of 0.51 s per block was used. A constant duration for each block was taken, to avoid the influence of the length of the block upon the autocorrelation.

Figure 5.26 shows the influence of dividing the signal in blocks of different duration. The difference between these functions is can be explained as follows: The duration of

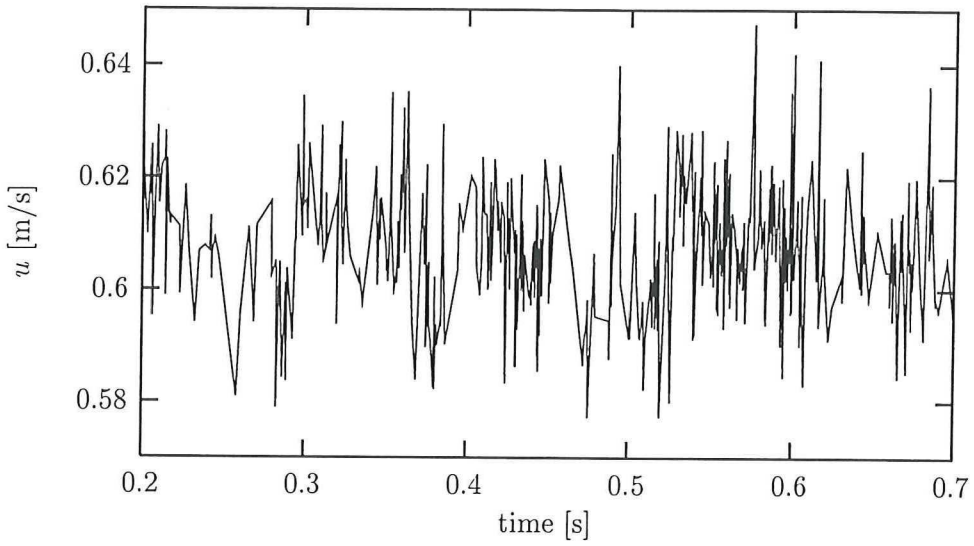

Figure 5.24: Characteristic velocity signal for case B.

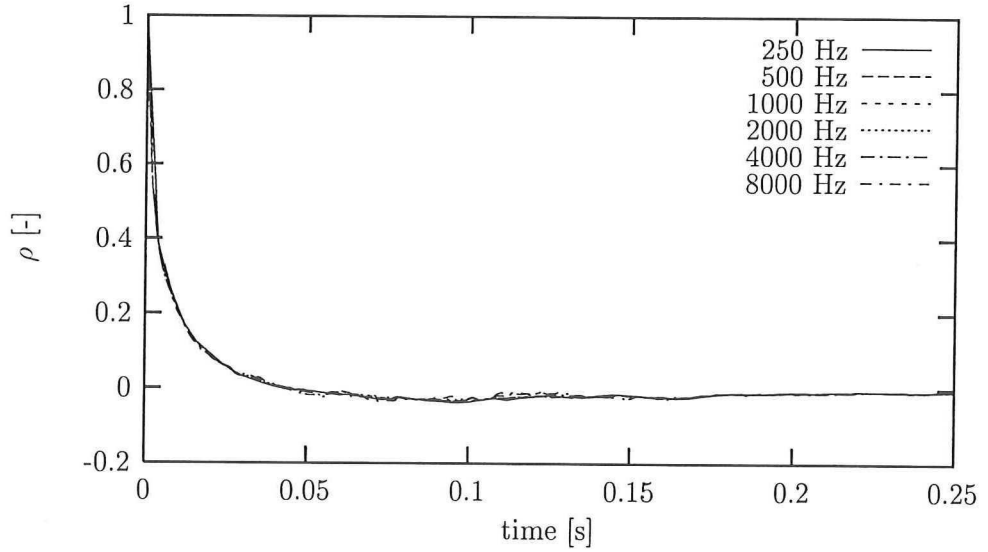

Figure 5.25: Autocorrelation function for case B, for different resample frequencies (mean data rate 827 Hz)

the block determines the maximum time, over which the correlation can be calculated. Low frequencies, present in the signal will result in a correlation over a long time. However, this will not be seen, if the duration of the blocks is shorter than the period of the low frequency. Thus a long block will show more correlation than a shorter one. That indeed low frequencies are present in the signal, is shown in Figure 5.27. For details is referred to Appendix D. Figure 5.27 shows a resonance frequency of the system at $\approx$ 0.07 Hz. The peak around 0.01 Hz is less reliable, because of the length of the blocks (102.4 s).
Because these low frequencies are of no interest (they are possibly caused by periodical fluctuations of the flow, induced by the pumps), small block are taken, to avoid this influence. Of course, the low resonance frequencies have their influence upon the integral time scale calculation. Taking 128 points per block for case A (according to a block time of 1.64 s) will give $\mathcal{T} = 8.02\ 10^{-3}$s, while 256 points per block (i.e. 3.28 s) gives $12.8\ 10^{-3}$ s.
For determining the integral time scale, the low frequency has to be filtered out first. The following summarising remarks can be made:

- No -5/3 slope is found in the spectra. In case A, this is probably caused by a too low data rate. Resampling with a low frequency will give a strong influence of aliasing (see Figure 2.3). This make the slope less steep. A high resample frequency includes a lot of information, which results in a -3.14 slope.
- Although case B has a higher data rate, no reliable information can be derived from this data set, because of the influence of multiple validation.
- No reliable integral time scale can be derived, caused by its dependency on the resample frequency, the number of blocks and the cutoff time.

To get reliable spectra, the following things should be taken into account:

- A sufficient high data rate is needed, to decrease the influence of the interpolation technique, and to be able to calculate the spectrum till at least the Kolmogorov frequency.

Table 5.5: Values for $\mathcal{T}$, for case B.

	250 Hz	500 Hz	1000 Hz	2000 Hz	4000 Hz	8000 Hz
$\sum_0^N \rho(\tau)\ d\tau$	$4.75\ 10^{-3}$	$3.63\ 10^{-3}$	$3.06\ 10^{-3}$	$2.80\ 10^{-3}$	$2.61\ 10^{-3}$	$2.50\ 10^{-3}$
$\sum_0^N \lvert\rho(\tau)\rvert\ d\tau$	$12.6\ 10^{-3}$	$11.1\ 10^{-3}$	$10.5\ 10^{-3}$	$10.2\ 10^{-3}$	$10.0\ 10^{-3}$	$9.94\ 10^{-3}$
$\sum_0^{T=0.4} \rho(\tau)\ d\tau$	$5.06\ 10^{-3}$	$3.93\ 10^{-3}$	$3.37\ 10^{-3}$	$3.11\ 10^{-3}$	$2.92\ 10^{-3}$	$2.82\ 10^{-3}$

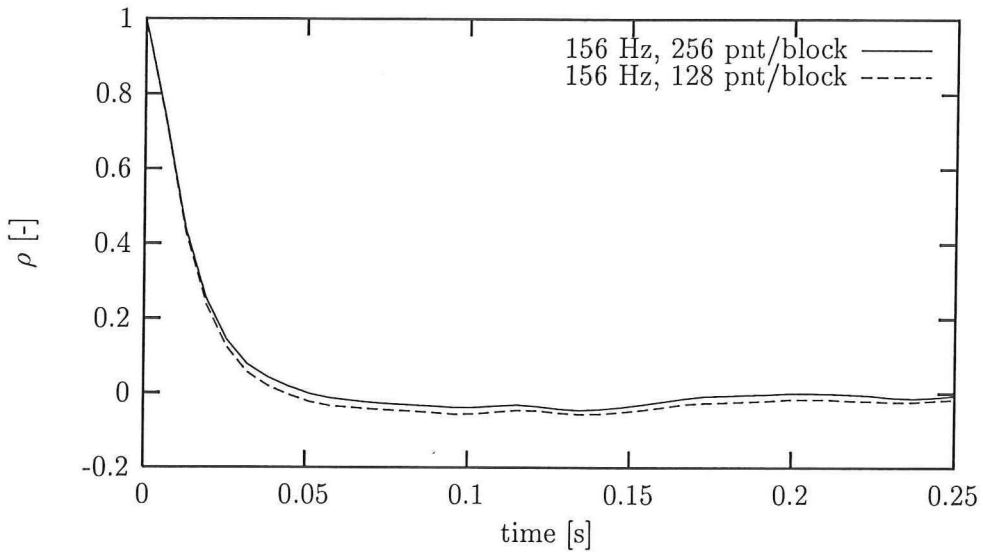

Figure 5.26: Influence of length of blocks upon the autocorrelation function (case A).

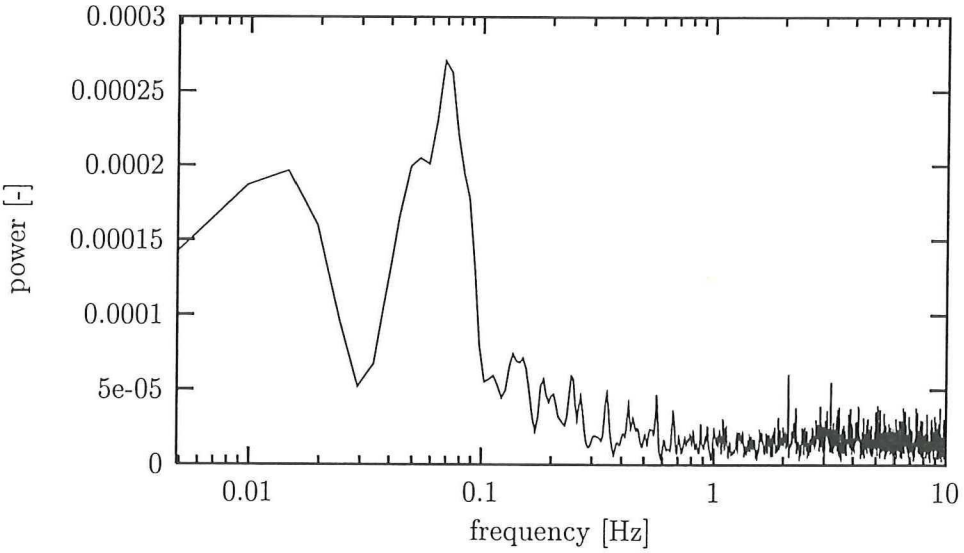

Figure 5.27: Spectrum for case A, for low frequencies

- A high frequency filter has to be applied, before resampling of the signal. This serves to prevent the influence of aliasing. Because of the random character of the inter particle arrival times, a discrete filter should be needed.

- Also a low frequency filter should be applied, to filter out the resonance frequency of the system, as seen in Figure 5.27. However, the possibility exists that this frequency depends on the amount of water in the system. To filter out all effects, an upper limit for the filter of $\approx$ 0.2 Hz is suggested.

5.6 Influence of bias corrections

Table 5.6: Comparison of different velocity bias correction methods (position (x,y,z) = (10,10.-12))

	U (m/s)	$\sqrt{u'^2}$ (m/s)	$\overline{v}$ (m/s)	$\sqrt{v'^2}$ (m/s)	$\overline{u'v'}$ (m^2/s^2)
number of points [k]	133		42		23
no correction	.5448	.0103	-.0089	.0141	-.000011
velocity	.5441	.0089	-.0091	.0140	-.000001
transit time	.5441	.0110	-.0094	.0141	-.000001

As mentioned in Section 3.1.2, several velocity bias correction methods exist. The mean, standard deviations and Reynolds stresses have been calculated using no bias correction, correction using the velocity or using the transit time. The results are given in Table 5.6. They have been measured at a point in the initial flow (i.e. (x,y,z) = (-10,10.-12) (cm)).
The following remarks can be made from Table 5.6:

- As expected, the corrected mean vertical velocity U is smaller than the not-corrected velocity, although the difference is negligible.
  However, this is not the case for $\overline{v}$. Perhaps, it is caused by the very small value for v.

- Also the standard deviations are influenced by the correction methods. The value for the velocity correction decreases, while the transit time method increases the calculated value, for $\sqrt{u'^2}$.
  The influence upon $\sqrt{v'^2}$ is small, because of the small value of v_n with respect to u_n (see equation 3.9).

- The correction methods have most influence upon the Reynolds shear stress. It decreases drastically, when using a correction method.

5.7 Sparger

As mentioned in Section 2.7 the air is driven out by the pressure drop over the tubes. Using a flow, corresponding to a gas fraction of 2 %, the pressure drops globally 50 Pa over a tube (according to equation 2.58). However, because the sparger is filled with water before air is injected, a minimal overpressure of $\rho g L$ ($\approx$ 250 Pa) has to be applied, to remove the water out of the tubes. What will happen, when the Poiseuille pressure drop is too small, is that only so many tubes will give air, till the pressure drop equals the gravity drop. This means that only a part of the tubes blows air, resulting in a non-uniform gas distribution.
Besides this effect, the surface tension (equation 2.62) implies a pressure drop of 300 Pa. So, even if all tubes are filled with air, only that number of tubes will be opened to bring the pressure drop by the Poiseuille flow to 300 Pa. To have all tubes working the pressure drop by friction has to be higher than the overpressure in a stagnant bubble cap [Lammers, 1994].
Instead of constructing a new sparger with smaller tubes, an other solution is applied, consisting of putting thin wires into each tube, with a thickens of 0.7 mm (in tubes with a internal diameter of 1 mm) resulting in a equivalent diameter of the tube of 0.46 mm, according to equation 2.61. This brings the Poiseuille pressure drop to approximately 1000 Pa. As no significant improvement was found with 0.8 mm wires, the 0.7 mm has been used, also because of the negative influence of chalk, that is present in the water. Some chalk precipitates upon, and even in the capillaries, and thus blocks these tubes, giving a negative influence upon the gas distribution. The investigations mentioned above, gave a big improvement of the gas distribution; before putting the wires, only the tubes till approximately 10 cm from the inlets formed bubbles, while after the changes, a (on the eye) an excellent distribution is seen. Figure 5.28 gives an impression of the situation, with $U_1 = 0.6$, $U_2 = 0.6$, $\alpha_1 = 2$ % and $\alpha_2 = 2$ %.

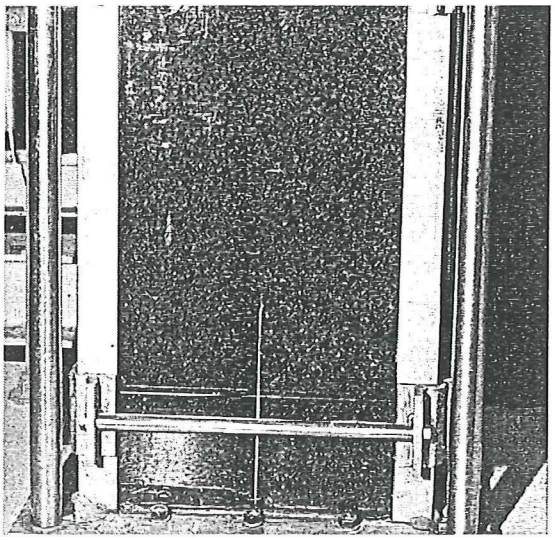

Figure 5.28: Photograph of the measuring section

Chapter 6

Recommendations

From the investigations the following are advised to be improved:

- To increase the data rate in the LDA experiments, different options are possible:
  - Seeding can be applied. Disadvantages are the high costs, because of the big amount needed for 10 m^3 of water, and the settling of seeding in the buffer vessel. In addition, the water must be refreshed regularly (because of the stain coming from the pumps) resulting in loss of the seeding.
    Another possible solution is the use of different scattering particles. Supply of milk powder is dissuaded because it stimulates the growth of algae in the system.
  - Rather than using the back scatter mode (see Section 4.2), forward scattering could be applied. At least in single phase measurements, a data rate of 1000 is realistic. Disadvantages of the present equipment are the laborious way of outlining, and a fluctuating preshift frequency.
- Probably, the effect of multiple validation is caused by the LDA system itself. Also other experimentators have detected this effect. Changes at the system should be executed to avoid multiple detection.
- Although the gas distribution has been improved by the wires, no optimal working of the sparger is obtained. Both visual observation and preliminary measurements point this out.
- A good traversing system is needed for the LDA system, fixed to the measuring section. It should allow traversing in both x and y direction. In addition, a vertical line above the splitter plate at the back wall is advised, to have a good zero-point determination in the y-direction.
- The holes for the fibre probes are too widely spaced to determine the gasfraction profiles as a function of the position. The following solutions are possible:
  - Construction of different probe shapes (as mentioned in Section 4.3). A disadvantage is the still poor measuring point distribution. It also gives problems with measuring a total profile, because the probes have to be moved

several times during the determination of a single profile. Apart from practical aspects (i.e the water has to be removed out the measuring section) the danger of damaging the fragile probes is realistic.

- Drilling holes in the side walls of the measuring section. This offers the possibility of measuring at arbitrary positions at one depth. A possible problem is the construction of the holes. Probably it 's not executable in glass. Using side walls of plexiglas could be a solution.

- The LDA signal has to be filtered. At first the low frequency of $\approx$ 0.07 Hz has to be removed. A possible way could be using a so-called the adaptive noise cancelling configuration [Van Vliet, 1997].
  The high frequencies (i.e. above the mean data rate) have to be filtered out as well (because of the aliasing effect, as mentioned in Section 2.6). This could be done by discrete filtering. A better solution is of course getting a data rate higher than the highest frequencies present in the flow.

- The maximal flow through the by-pass loops is too small, resulting in a small range of velocity differences between the two sections. The maximal difference amounts $\pm$ 30 cm/s.
  By using other valves with less friction, the flows can be regulated in a wider range.

- To get a more isotropic initial flow, a longer stabilisation period is needed. A possibility is lengthening the splitter plate, and measuring in the section what is now above the measuring section. That section is made out of plexiglas. This also gives the possibility of drilling holes for the fibre probes in the side walls.

- The pumps have to be treated against stain, which now dramatically contaminates the water. This makes it neccesary to refresh the water regularly. The only circumstance in which the use of seeding particles makes sense, is obtained when the pumps are treated, demineralized water is used, and the whole system is protected against contaminations.
  These contaminations are not only dust etc, but can also be algae. Algae growth can be slowed down by covering the setup against light, when no measurements are done. Proposed is the placing of a curtain around the measuring section, to open and cover it easily.
  Algae growth also decreases by a continuous supply of air via the sparger. Besides a high oxigen percentage in the water, the circulation through the whole setup decreases the growth.

Chapter 7

Conclusions and recommendations

7.1 Conclusions

- The initial flow is constant in time within 1.5 %.
  Because of leakage between the two sections, no accurate flow estimate in the measuring section can be made from the flow meters.
- The initial vertical turbulence intensity I_x amounts to 2 %.
- The dimensionless description of the velocity profiles is indicative of a well-developed mixing layer.
- The data rate for the LDA measurements is too low for spectral analysis. Futher, multiple validation of the scattering particles has a negative impact upon the reliability of the spectrum.
- The gas distribution was improved by inserting wires in all capillaries of the sparger.
- The turbulence in the initial flow can be considered as grid-generated.

7.2 Recommendations

- The data rate in the LDA experiments has to be imcreased.
- A stable traversing system for the LDA system is needed.

For a more comprehensive overview of the recommendations, the reader is referred to Chapter 6.

Bibliography

Absil, L. H. J., (1995), Analysis of the laser Doppler measurement technique for application in turbulent flows: Ph.D. thesis, Delft University of Technology, The Netherlands.

Adrian, R. J., and Yao, C. S., (1987), Power spectra of fluid velocities measured by laser Doppler velocimetry: *Experiments in Fluids*, **5**, 17–28.

Bradshaw, P., (1971), *An introduction to turbulence and its measurements*: Pergamon Press.

Brown, G. L., and Roshko, A., (1974), On density effects and large structure in turbulent mixing layers: *Journal of Fluid Mechanics*, **64**, no. 4, 775–816.

Cartellier, A., (1990), Optical probes for local void fraction measurements: Characterisation of performance: *Rev. Sci. Instrum.*, **64**, no. 2, 874–886.

Doelman, M. S., (1997), Three-dimensional phase-resolved laser Doppler measurements in a stirred tank: Masters's thesis, Delft University of Technology, The Netherlands.

Ellingsen, K., and Roig, V. e. a. Improvements of velocity measurements in bubbly flows by comparison of simultaneous hot-film and LDA signals:. ASME Fluids Engineering Division Summer Meeting, (1997).

Guenter, R., (1990), *Modern Optics*: John Wiley & son Ltd.

Janssen, L. P. B. M., and Warmoeskerken, M. M. C. G., (1991), *Transport phenomena data companion*: Delft, Delftse Uitgevers Maatschappij.

Lammers, J. H., (1994), The stability of bubbly flows: Ph.D. thesis, University of Twente, The Netherlands.

Lance, M., and Bataille, J., (1991), Turbulence in the liquid phase of a uniform bubbly air-water flow: *Journal of Fluid Mechanics*, **222**, 95–118.

Maanen, H. R. E. v. Signaalprocessen en Signaalverwerking voor LDA:. Tweede-fase cursus Laser Doppler Anemometrie van het Burgerscentrum, (1996).

Marié, J. L., (1983), Investigation of two-phase bubbly flows using Laser Doppler Anemometry: *PhysicoChemical Hydrodynamics*, **4**, no. 2, 103–118.

Mulder, A. R., (1996), Gemiddelde en tijdsafhankelijke stromingsverschijnselen in bellenkolommen: Masters's thesis, Delft University of Technology, The Netherlands.

Nieuwstadt, F. T. M., (1992), *Turbulentie*: Utrecht, Epsilon Uitgaven.

Priestley, M. B., (1975), *Spectral analysis and time series*: England: Academic press limited.

Roig, V., (1993), Zones de mélange d'écoulements diphasique à bulles.: Ph.D. thesis, Institute de Mécanique des Fluides de Toulouse.

Sheng, Y. Y., and Irons, G. A., (1991), A combined LDA and electrical probe diagnostic for bubbly two-phase flow: *Int. Journal of Multiphase Flow*, **17**, no. 5, 585–595.

Tennekes, H., and Lumley, J. L., (1972), *A first course in turbulence*: Cambridge, The MIT Press.

Theofanous, T. G., and Sullivan, J., (1982), Turbulence in two-phase dispersed flows: *Journal of Fluid Mechanics*, **116**, 343–362.

Tummers, M. J., and Passchier, D. M., (1996), Spectral analysis of individual realization LDA data: *Technical Report LR 808.*

Calibration certificate IFS4000.

Users manual Kompakt-Durchfluβmesser K300.

Van den Akker, H. E. A., Fysische Technologie van Conversieprocessen en Produktbewerkingen:, (college dictate), (1997).

Van der Haagen, T. H. J. J. Noise analysis, Basics & practice:. Summer school of the Burgerscentrum on Experimental techniques in Multi-Phase Flow, (1995).

Van Vliet, E., (1997), An LDA study of the precessing vortex core in cyclone: Masters's thesis, Delft University of Technology, The Netherlands.

Appendix A

Specifications of the LDA settings

The dimensions of the measuring volume, according to the different colours and focal lengthes of the lenses, are given in Table A.1, while the fringe spacings are given in Table A.2.

Table A.1: Dimensions of the probe volumes in water as a function of the lens and wavelength.

F [mm]	**250**	**350**	**500**
Θ [°]	4.281	3.0602	2.1434
Green			
d_0 [10^-6 m]	68	95	135
d_m [10^-6 m]	68	95	135
l_m [10^-6 m]	904	1770	3607
Blue			
d_0 [10^-6 m]	64	90	128
d_m [10^-6 m]	64	90	128
l_m [10^-6 m]	857	1678	3422
Violet			
d_0 [10^-6 m]	62	87	125
d_m [10^-6 m]	63	88	125
l_m [10^-6 m]	836	1637	3338

Table A.2: Fringe spacings d_f [10^{-6} m] in water as a function of the lens and wavelength.

F [mm]	**250**	**350**	**500**
Θ [°]	4.281	3.0602	2.1434
Green	2.585	3.611	5.151
Blue	2.452	3.425	4.886
Violet	2.392	3.340	4.766

Appendix B

Specifications of water flow meters

For the water flow measurements, Krohne Altometers, types IFS4000 and K300 are used. Their measuring method is based on the magnetic induction caused by the flow, as a response to an applied magnetic field [Users manual K 300,] and [Users manual IFS4000,]. The IFS4000-type displays the flow in lit/min. To calculate the theoretical value of the velocity in the measuring section, the following equation can be used:

$$U_2 = \frac{1}{60} \frac{\text{flow in lit/min}}{\text{surface of measuring section}} = \frac{\text{flow in lit/min}}{2400} \tag{B.1}$$

The deviations of the IFS4000 type are given below. The 100 % range accords with 1413.7 lit/min. Remind that flows higher than this value are measured.

Range in %	Deviation in %
99	0.024
50	-0.30
22	0.08

The K300-type shows a value between 0 and 1 Volt, where 1 Volt corresponds to a mean velocity through the flowmeter of 1, 2, 4, or 8 m/s respectively, dependent on the used range. For the 1 m/s range, which is used in the experiments, the following relation between the voltage, and the mean velocity in the measuring section holds:

$$U_1 = \frac{\text{surface of flow meter}}{\text{surface of measuring section}} * \text{velocity in flow meter} = \frac{\pi}{4} * \text{velocity} \tag{B.2}$$

The voltage is measured with a Fluke 77 multimeter.

For the K300 type the error ranges are:

Range in %	Deviation
0..20 %	$\pm$ 1 % of end value
20..100 %	$\pm$ 0.2 % of measured value

Measuring the velocity with the LDA-system, and comparing it with the flow according to the flowmeters, gives Figure B and B. The velocities are measured at the positions

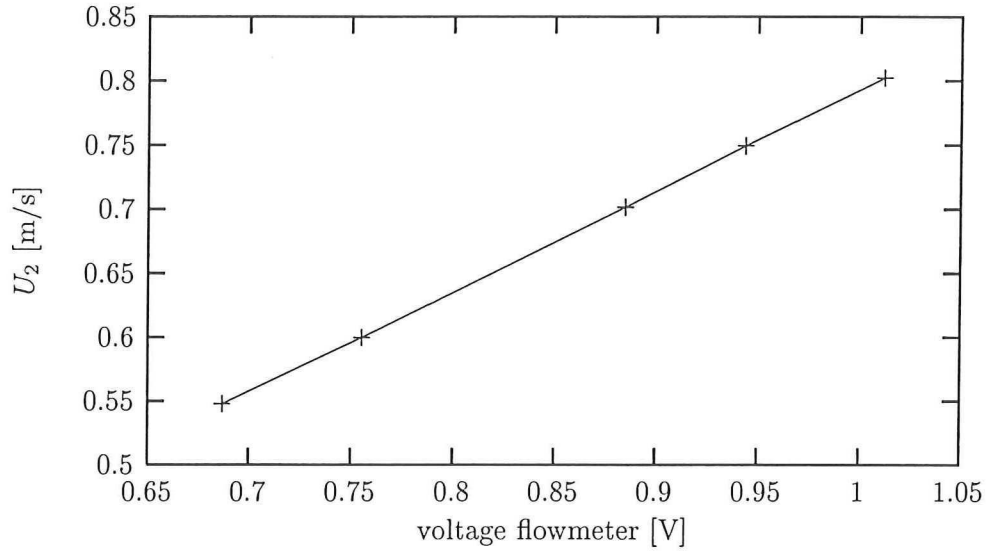

Figure B.1: Calibration curve for the Krohne K300.

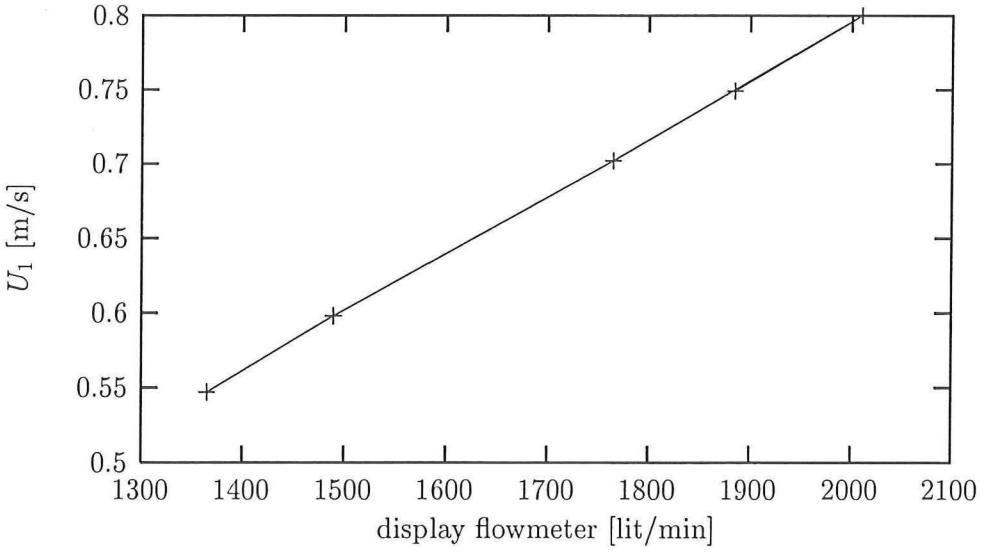

Figure B.2: Calibration curve for the Krohne IFS4000.

(x,y,z) = (10,-10,-12) and (10,10,-12). These figures are determined with the same velocities at both sides, to avoid the influence of the leakage. The values for the fitted lines of the form $y = ax + b$, with the error intervals, are given in Table B.1. The

Table B.1: Fitted values of the calibration curves for the water flow meters.

	a (m/sV)	δ a (m/sV)	b (m min/lit s)	δ b (m min/lit s)
U_1	$3.89\ 10^{-4}$	$2.3\ 10^{-6}$	0.016	0.004
U_2	0.7857	0.0030	0.0075	0.0026

deviation from the theoretical values is 7 % for U_1 (2400 * $3.89\ 10^{-4}$), and 0.04 % for U_2 ($0.7857/\frac{\pi}{4}$). A possible reason for the big deviation for U_1, could be that the measuring position for the LDA is not a representable place, because of the depth dependance at that section.

Appendix C

Calibration of air flow meters

For the determination of the air flow, Fischer $ Porter precision bore flow rate tubes, types 3f-3/8-20-5/36 and FP-3/0-0-5/36, are in use. Their flow ranges are 36 and 64 lit/min respectively. The error is estimated as 0.2 lit/min. The calibration curves, depicted in Figure C.1 and C.2 are measured: The values for the straight line fitting ($y = ax + b$) are given in Table C.1:

Table C.1: Specifications of the laser Doppler anemometer.

	a (m^3/s)	δ a (m^3/s)	b (m^3/s)	δ b (m^3/s)
3f-3/8-20-5/36	2.99164 10^{-5}	3.99682 10^{-7}	-1.6308 10^{-5}	5.02126 10^{-6}
FP-3/0-0-5/36	4.68578 10^{-5}	6.20288 10^{-7}	-3.78198 10^{-5}	1.05834 10^{-5}

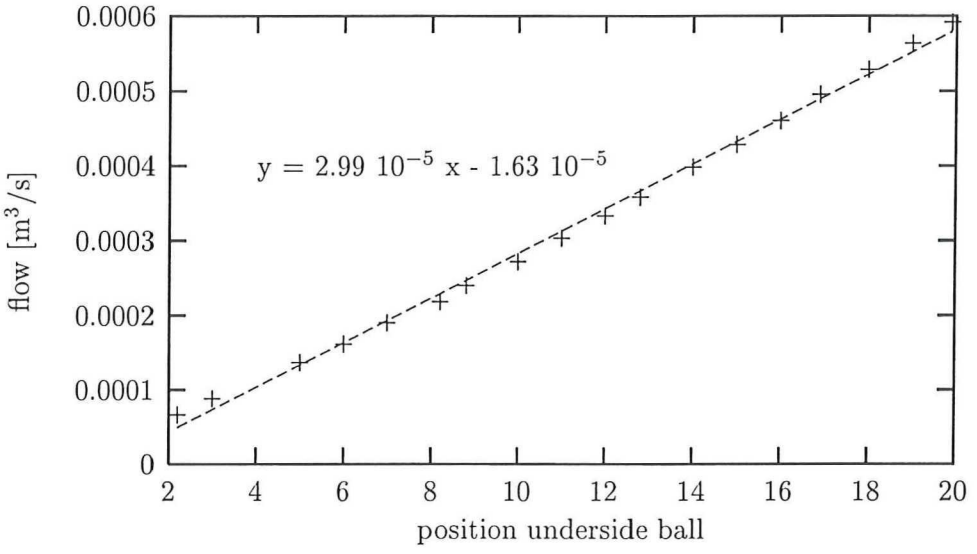

Figure C.1: The calibration curve for the 3f-3/8-20-5/36

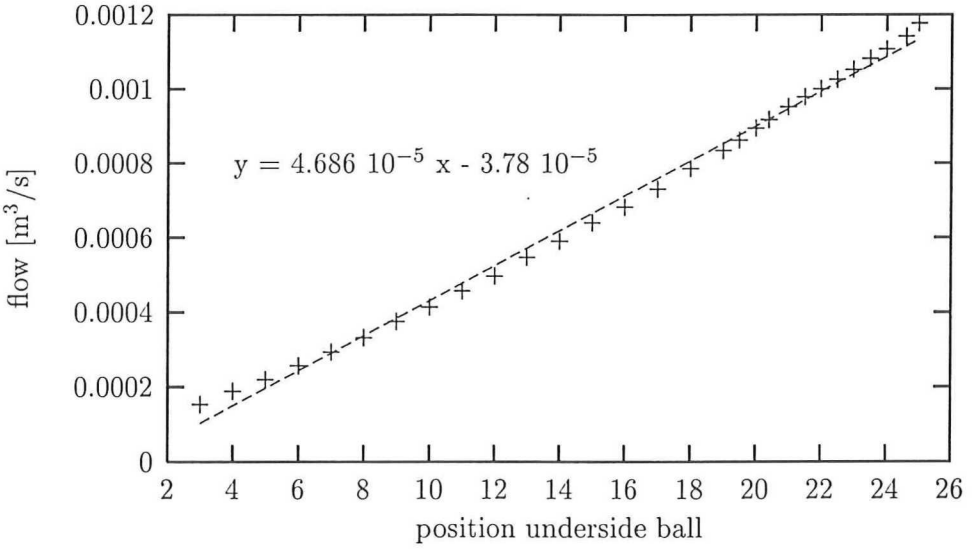

Figure C.2: The calibration curve for the FP-3/0-0-5/36

Appendix D

Specifications of spectrum calculations

As mentioned in Section 2.6, for a more accurate calulation of the spectrum and the autocorrelation function, the resampled signal is divided in blocks.

The following division in blocks is made for case A(Figure 5.18):

The measuring position is at (x,y,z) = (10,10,-12) (cm). The mean velocity is 0.608 m/s, and the standard deviation amounts 0.011 m/s.

Table D.1: Specifications for case A.

resample frequency [Hz]	156	1248	2496	4992
number of blocks	389	150	150	74
points per block	256	2048	4096	8192
time per block [s]	1.64	1.64	1.64	1.64

For case B (Figure 5.22) holds:

Table D.2: Specifications for case B.

resample frequency [Hz]	250	500	1000	2000	4000	8000
number of blocks	465	465	465	465	269	48
points per block	128	256	512	1024	2048	4096
time per block [s]	0.51	0.51	0.51	0.51	0.51	0.51

Its measuring position is at (x,y,z) = (10,10,69). The mean velocity amounts 0.606 and its standard deviation 0.015.

For Figure 5.27 holds:

Table D.3: Specifications for Figure 5.27.

resample frequency [Hz]	20
number of blocks	6
points per block	2048
time per block [s]	102.4

Because of the low number of blocks, the accuracy is small, but it is assumed that this has no influence on the position of the peak. Figure 5.27 is determined with the data of case A.

Appendix E

Accuracies of calculated quantities

To get an idea of the accuracy of the calculated mean and fluctuating velocity, an estimate of the error due to finite measuring time can be made.

Mean velocity For the difference between the calculated and real mean velocity holds [Tennekes and Lumley, 1972]:

$$U_T - U = \frac{1}{T}\int_0^T [u(t) - U]\, dt = \frac{1}{T}\int_0^T u'(t)\, dt \tag{E.1}$$

Then the mean square value is:

$$\overline{(U_T - U)^2} = \frac{\overline{u'^2}}{T^2}\int_0^T\int_0^T \rho(t' - t)\, dt\, dt' = \frac{2\overline{u'^2}}{T}\int_0^T \left(1 - \frac{\tau}{T}\right)\rho(\tau)\, d\tau \tag{E.2}$$

Assuming that $\tau/T \approx 0$ if $\rho(\tau) \neq 0$, results in:

$$\overline{(U_T - U)^2} \cong 2\overline{u'^2}\mathcal{T}/T \tag{E.3}$$

With a measuring time T of $\pm$ 100 s (from Table 5.1), the error in the determination of U due to an limited measuring time is negligible (i.e 2 10^{-5} m/s). However, also an inaccuracy due to the fluctuations in the flow of the pumps is present.

Variance accuracy The inaccuracy in the calculated variance due to the turbulent motion can be estimated as follows [Priestley, 1975, page 327]:

$$var\{\sigma^2\} = var\{\hat{R}(0)\} \simeq \frac{2\mathcal{T}}{T}\sum_{m=-\infty}^{\infty} R^2(m) = \frac{2\sigma^4}{T}\sum_{m=-\infty}^{\infty}\rho^2(m) \tag{E.4}$$

Using $\sum_{m=-\infty}^{\infty}\rho^2(m) \leq \left(\sum_{m=-\infty}^{\infty}|\rho(m)|\right)^2$, and the fact that $\rho(\tau)$ is an even function, equation E.4 can be rewritten to:

$$var\{\hat{R}(0)\} \leq \frac{4\sigma^4\mathcal{T}}{T}\left(\sum_{m=0}^{\infty}|\rho(m)|\right)^2 \tag{E.5}$$

Using a value of 25 10^{-3} s for $\sum_{m=0}^{\infty}|\rho(m)|$ (from Table 5.4), this inaccuracy is negligable (i.e. $10^{-12}m^2/s^2$).

Total water flow For the accuracy in Φ (equation 5.1) holds:

$$(\delta\Phi)^2 \simeq \sum_{i=1,j=1}^{i=17,j=9} (\delta U_{i,j})^2 * L\ B^2 \simeq 7 * 9 * (0.2 * 0.2)^2 * (\delta U)^2 \qquad \text{(E.6)}$$

With L and B the dimensions of the section.
To make a real estimate for δU, the mean velocity for different times is given in Figure E.1. As can be seen, the total inaccuracy after 100 s is approximately 0.001 m/s. This

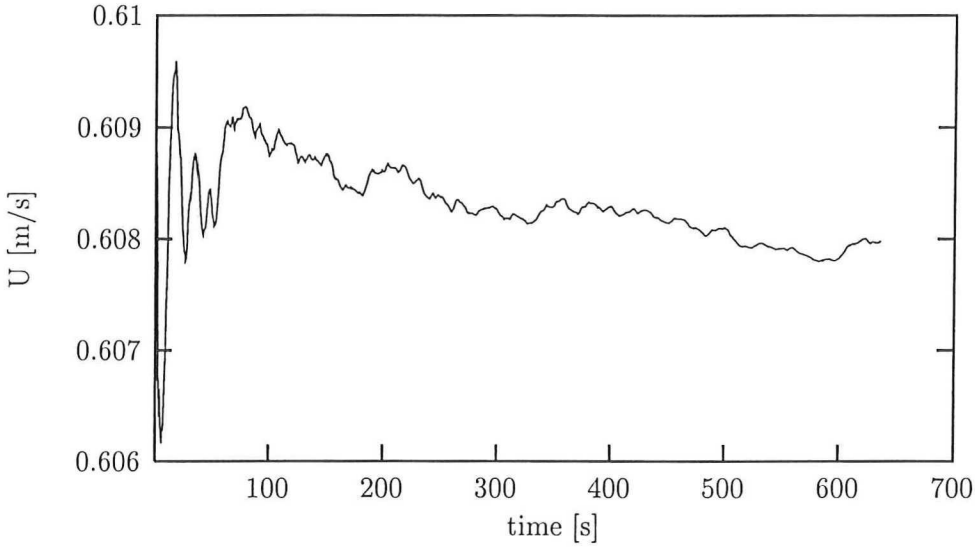

Figure E.1: Mean velocity for case A

can be taken as a measure for δU. Equation E.6 then gives that $\delta\Phi \sim 30$ lit/min.
The fluctuating velocity as a function of time is depicted in Figure E.2.

Figure E.1 and E.2 show that, after a measuring time of 100 s, the mean velocity is deviates 0.2 %, and the fluctuating velocity 3 % from the final value.
For a measuring time of 1 minute, the mean is constant within 0.5 % and the variance within 4 %. These estimates are done by calculating the mean and variance over blocks of 1 minute, and considering the maximum difference between the values for different blocks.
Figure E.1 seems to show a decrease in velocity of 1 mm/s for 500 s.

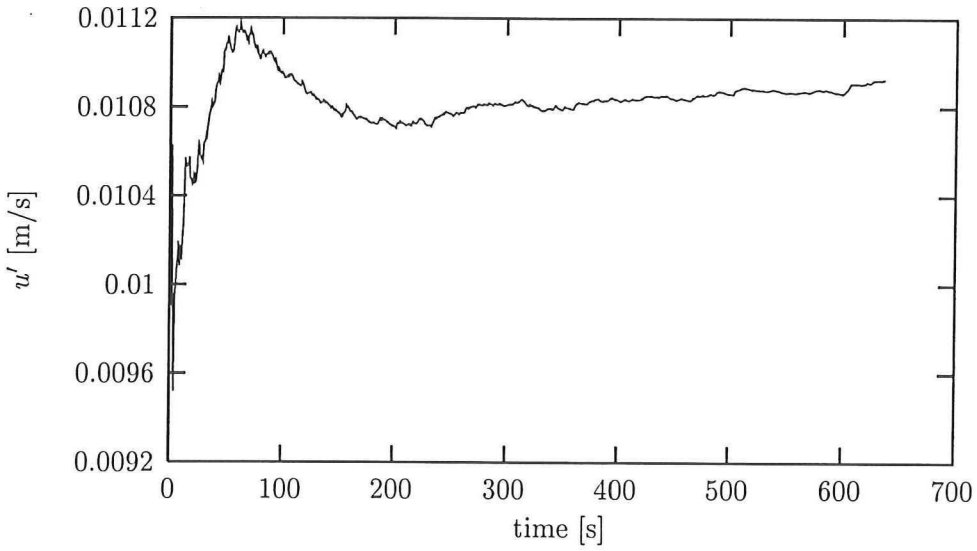

Figure E.2: Fluctuating velocity for case A